Formation and Diagenesis of Sedimentary Rocks in Gale Crater, Mars

Thesis by
Kirsten L. Siebach

In Partial Fulfillment of the Requirements for
the degree of
Doctor of Philosophy

CALIFORNIA INSTITUTE OF TECHNOLOGY
Pasadena, California

2016
(Defended May 19, 2016)

Kirsten L. Siebach
ORCID: 0000-0002-6628-6297

ACKNOWLEDGEMENTS

First, I would like to thank my advisor, John Grotzinger, for research and advising support over the last five years. I have greatly appreciated the chance to learn from his impressive example as a scientist, a leader, and as a field geologist, and for the opportunities he has given me to work on missions, to present and connect with other scientists, and to travel and get to see and learn about amazing rocks around the world. I would also like to thank Bethany Ehlmann for her mentorship, friendship, example, and helpful advice through several classes and years of group meetings. I am grateful to Paul Asimow and Mike Lamb for guidance on my first year project, advice on classes and graduate school, and for both of their examples as inspiring teachers, and to Ken Farley for his help and perspective on my thesis committee.

I have benefitted greatly from scientific and personal interactions with collaborators and mentors from the MSL science team—thanks particularly to Linda Kah, Scott McLennan, and Mike Baker, for very helpful discussions. A special thanks to Ray Arvidson, without whose advice and mentorship I would not be where I am today.

It has been a privilege to work with and learn from the faculty, staff, and students at Caltech. I want to thank the Grotzinger and Ehlmann groups, especially Jennifer Shechet, Katie Stack-Morgan, Melissa Rice, and Jennifer Buz, for discussions, friendship, and advice throughout graduate school, and helpful group meetings. I am also grateful to the wonderful staff members in the GPS division, especially Janice Grancich, Marcia Hudson, and Liz Boyd—I always leave your offices with a smile, thank you.

I cannot imagine how I would have finished the last five years without the incredible support I have had from my friends. Thanks to Mathieu Lapôtre, Pablo Guerrero, Morgane Grivel, and Abigail Fraeman, for meal breaks and countless miles of walking and discussions. Thanks to Sarah Slotznick for four years of excellent officemate chats and chocolate. Thanks to Caltech LDSSA for carpools, conversations, and ice cream adventures.

Finally, I would especially like to thank my family—my parents, Paul and Gretchen Siebach, my sister Chloe, and brother Jeffrey for their constant, endless love and support. Thanks for always answering the phone. I couldn’t have done it without you.

ABSTRACT

The history of surface processes on Mars is recorded in the sedimentary rock record. Sedimentary rock layers exposed in Gale Crater on the modern crater floor (Aeolus Palus) and on Mount Sharp (Aeolus Mons), which hosts one of the more complete records of transitions between major mineralogical eras on Mars, have been investigated by the Mars Science Laboratory *Curiosity* rover since landing in August 2012. This dissertation focuses on the formation and diagenesis of the sedimentary rocks in Gale crater in order to assess the compositional diversity of the volcanic sources around Gale crater, the effects of transport processes on the sediment grains, and the volumes and geochemistry of water that transported and cemented the sediments. The first study uses orbital mapping of a distinctive cemented boxwork layer on Mount Sharp to constrain a minimum volume of groundwater available to form this layer, 1 km above the modern floor of Gale, with implications for the formation of Mount Sharp. The other three studies use *Curiosity* rover imagery and geochemical data to investigate sedimentary rocks in Aeolus Palus and at the base of Mount Sharp. The second study identifies and describes diagenetic synaeresis cracks in the Sheepbed mudstone, at the lowest elevation in Aeolus Palus, with implications for the duration of water saturation of these lake sediments. The third and fourth studies identify and explain geochemical trends in the fluvio-deltaic Bradbury group, the Murray mudstone formation, and the eolian Stimson sandstone, focusing on geochemical diversity in the source regions for each of these units and how different depositional processes are reflected in the geochemical data. The sedimentary system in Gale crater has changed our understanding of Mars by expanding the known variety of igneous rocks, increasing estimates of the longevity of surface water lakes, and showing that there were once habitable environments on our neighboring planet.

PUBLISHED CONTENT

Chapter 2 is published in:

Siebach, K. L., and J. P. Grotzinger. (2014) Volumetric Estimates of Ancient Water on Mount Sharp Based on Boxwork Deposits, Gale Crater, Mars. *J. Geophys. Res.,* online 28 Jan 2014, doi: 10.1002/2013JE004508.

Chapter 3 is published in:

Siebach, K. L., J. P. Grotzinger, L. C. Kah, K. M. Stack, M. Malin, R. Leveille, and D. Y. Sumner. (2014) Subaqueous Shrinkage Cracks in the Sheepbed Mudstone: Implications for Early Fluid Diagenesis, Gale Crater, Mars. *J. Geophys. Res.*, online 17 Jul 2014, doi: 10.1002/2014JE004623.

TABLE OF CONTENTS

LIST OF TABLES AND FIGURES

ACRONYMS

APXS. Alpha Particle X-Ray Spectrometer

BF. Bright Fractured unit

ChemCam. Chemistry and Camera

CheMin. Chemistry and Mineralogy

CIA. Chemical Index of Alteration

CTX. Context Camera

DTM. Digital Terrain Model

EP. Expected vertical Precision

GEL. Global Equivalent Layer

GIS. Geographic Information System

HiRISE. High Resolution Imaging Science Experiment

LIBS. Laser-Induced Breakdown Spectroscopy

MAHLI. MArs Hand Lens Imager

MARDI. MARs Descent Imager

MastCam. Mast Camera

MOLA. Mars Orbital Laser Altimeter

MSL. Mars Science Laboratory

NASA. National Aeronautics and Space Administration

Navcam. Navigation Camera

PDS. Planetary Data System

RDR. Reduced Data Record

THEMIS. Thermal Emission Imaging System

TIN. Triangulated Integrated Network

USGS. United States Geological Survey

XRD. X-Ray Diffraction

Chapter 1

Introduction

1.1 Sedimentary Records on Earth and Mars

The sedimentary rock record contains the history of the changing surface of the planets. Sediments can be transported whenever the wind blows or water moves, and, when these sediments accumulate and are preserved as rock, they record the story of their formation: the accumulated grains reveal the type of rocks that were upstream or upwind, the size and shape of the grains indicates the manner in which they were deposited, fossils preserve remains of life, chemical weathering of grains relates to the climate, cementation that turns grains into rock reveals the groundwater chemistry, and cracks or fractures tell the story of stresses applied to the rock and the environment when they healed. Studying the sedimentary rocks therefore enables us to tell the story of a location, and in some cases, the story of the planet. Planet-scale changes can be recorded globally in the rock record from that time; on Earth, the geochemistry of marine shales records — to name a few examples — the evolution of continental crust [*Taylor and McLennan*, 1995], the oxidation of the atmosphere due to photosynthesis [*Canfield*, 2005; *Falkowski and Isozaki*, 2008], major extraterrestrial impacts [*Alvarez et al.*, 1980], and the uplift of the Himalayas [*Palmer and Edmond*, 1989]. On Mars, we seek understanding of both local and global phenomena through our study of the sedimentary rock record.

Until recently, it was unclear whether Mars even had a sedimentary record—the planet today is dry and the lack of plate tectonics implies a lack of the burial and uplift processes typical of sedimentary rock formation on Earth [e.g. *Worden and Burley*, 2003]. Sediment production on Mars was suggested based on observations of channels [*Sharp and Malin*, 1975], windblown sediment [*McCauley*, 1973], and layered deposits [*Murray et al.*, 1972; *Soderblom et al.*, 1973] in early Mariner 9 imagery, but the presence of a sedimentary record was not established until a seminal paper by Malin and Edgett in 2000, which used Mars Orbital Camera images to identify and describe sedimentary deposits distributed across the surface of Mars [*Malin and Edgett*, 2000]. A few years later, the volume and

resolution of data available increased exponentially with a series of successful orbiter and rover missions, providing confirmation of the presence of significant sedimentary deposits from both rover [*Squyres et al.*, 2004; *Grotzinger et al.*, 2005; *McLennan et al.*, 2005] and orbital [*Jerolmack et al.*, 2004; *Fassett and Head*, 2005] perspectives, and evidence for their association with water-lain minerals [*Bibring et al.*, 2005; *Poulet et al.*, 2005; *Bibring et al.*, 2006; *Ehlmann et al.*, 2008a; *Ehlmann et al.*, 2008b; *Mustard et al.*, 2008].

Now that the presence of a sedimentary record in Mars has been established [*Malin and Edgett*, 2000; *McLennan and Grotzinger*, 2008b; *Grotzinger and Milliken*, 2012], we seek to understand the episodes of global change through time that are recorded therein. While specific changes are best observed at the rover-scale, site selection must be accomplished based on global trends, established by orbital observations. Martian surfaces are dated based on the density of craters, calibrated (with considerable uncertainty) by comparison with cratered surfaces on the moon, from which we have samples that have been radiometrically dated [*Hartmann and Neukum*, 2001]. Mars offers a unique record compared to Earth because most of the Martian sedimentary rock record is more than 3 billion years old [*Tanaka et al.*, 2014], whereas it is difficult to find unmetamorphosed ancient sedimentary rocks on Earth. Bibring et al. [2006] pointed out that, to first order, the orbitally-mapped mineralogies of Martian rocks are related to their age, where phyllosilicate clays are most often associated with the oldest Noachian-era surfaces (4.5-~3.8 Ga), sulfates and other salts are associated with Hesperian-era surfaces (~3.8-3.3 Ga), and dry dusty iron-oxides are associated with Amazonian surfaces (~3.3 Ga-present) [*Bibring et al.*, 2006; *Ehlmann and Edwards*, 2014]. While this scheme is simplified, it highlights major mineralogical changes worth investigating in the sedimentary record; perhaps the transitions between these clay-rich, salty, and dry eras will reveal the global changes that shaped Mars. Furthermore, phyllosilicate clays are of special interest because of their potential for preserving organic molecules. At the time when landing sites for Mars Science Laboratory (MSL) were being chosen, only one site was found where rover-accessible layered sedimentary deposits recorded the transitions between phyllosilicates, sulfate-rich deposits, and iron oxides [*Grotzinger and Milliken*, 2012], so the Gale crater

site was selected for further investigation of the sedimentary record of environmental transitions on Mars.

1.2 Gale Crater

Gale crater is a 154 km-diameter crater sitting on fluvially-dissected Noachian terrain along the dichotomy boundary that divides the southern highlands from the northern lowlands of Mars. It is an example of a class of craters identified and mapped by Malin and Edgett as a partially-filled crater with layered interior deposits, which in this case form a mound that extends higher than the northern crater rim [*Malin and Edgett*, 2000]. This mound likely surrounds the crater's central peak and, based on other similar craters, is likely an erosional remnant from a more complete crater fill [*Malin and Edgett*, 2000; *Grotzinger et al.*, 2015]. The layers exposed on the mound, called Mount Sharp (formally Aeolus Mons), were mapped in higher resolution by Anderson and Bell [2010] and the mineralogy associated with each layer was described in Milliken et al. [2010] in anticipation of Gale crater being a potential landing site for MSL.

Mount Sharp is just over 5 km tall, and has a significant unconformity about 1.3 km above the modern crater floor that separates the lower formation from the upper formation. The lower formation includes a thin phyllosilicate clay-bearing layer about 100 m above the base of the mound and a thick sequence of sulfate-bearing layers above the phyllosilicates [*Milliken et al.*, 2010]. In addition to these mineralogical indicators of water-rich sedimentation, there are channels indicating water flow from the base of the unconformity to the bottom of the mound, and a variety of fluvial channels leading into the crater [*Anderson and Bell*, 2010; *Palucis et al.*, 2014]. Within the sulfate-bearing layer, about 1 km above the floor of the mound, there are boxwork deposits that were identified by Anderson and Bell [2010] and are discussed in detail in Siebach and Grotzinger [2014a] (Chapter 2), which require significant volumes of groundwater to have fluxed through at this elevation of Mount Sharp. The MSL rover *Curiosity* landed on the floor of the crater, called Aeolus Palus, and has traversed to the base of Mount Sharp and up through about 40 meters of the stratigraphy, but has not yet (as of May, 2016) reached the phyllosilicate-bearing unit identified from orbit.

1.3 Mars Science Laboratory

The Mars Science Laboratory *Curiosity* rover is the most complex rover ever sent to the surface of Mars. It is 900 kg, 2.2 m tall, has a 1.9 m long robotic arm, and has eleven science instruments for in-situ data collection and analysis. Of relevance to the work presented here, these include stereo black and white navigation cameras (NavCam); stereo true-color mast cameras (MastCam); a Laser-Induced Breakdown Spectrometer (LIBS; ChemCam instrument) for remote compositional analyses at fine resolution; a robotic arm equipped with a drill for sampling, a high-resolution camera (MAHLI), and an Alpha-Particle X-ray Spectrometer (APXS) for quantitative compositions of 1.7-cm diameter spots; and an X-Ray Diffractometer (XRD) for crystalline mineralogy in the Chemistry & Mineralogy experiment onboard (CheMin) [*Grotzinger et al.*, 2012].

Since *Curiosity* successfully landed at Bradbury Rise in Aeolus Palus on 6 August 2012, *Curiosity*'s operations on Mars have been directed by the ~500 member MSL Science and Operations team on Earth. Work for this thesis incorporates *Curiosity*'s observations through sol 1300 (i.e., April 3, 2016).

1.4 Thesis Summary

Gale crater has been identified as one of the key sedimentary sections on Mars since sedimentary rocks were identified on that planet [*Malin and Edgett*, 2000]. With detailed orbital imagery and significant volumes of rover data now available for Gale crater, we are able to investigate the sedimentary record of Mars in unprecedented detail. The chapters in this thesis are designed to understand the formation and diagenesis of the sedimentary rocks in Gale crater encountered during each stage of the MSL mission.

Prior to *Curiosity*'s landing, orbitally-based imagery was used to map an extensive layer of boxwork deposits in Mount Sharp, which are discussed in chapter 2 with implications for the formation of the mound itself and the importance of groundwater. After landing, *Curiosity* drove to and investigated the lowest elevation unit in the floor of Aeolus Palus, which was a mudstone called the Sheepbed formation. Chapter 3 is a detailed investigation of diagenetic synaeresis cracks in the mudstone, which contributed to the

interpretation of the Sheepbed formation as a once-habitable lake environment [*Grotzinger et al.*, 2014]. After investigating the Sheepbed mudstone, *Curiosity* drove another 9 km across Bradbury group fluvio-deltaic sediments exposed in Aeolus Palus. Chapter 4 presents a grain-size based classification scheme for the Bradbury group rocks analyzed by *Curiosity* and shows that the geochemistry of these rocks is mostly related to mineral sorting based on grain size during fluvial transport. On sol 750 (i.e., September 14, 2014), *Curiosity* reached the base of Mount Sharp and began investigating the Murray formation, another mudstone formed in an ancient lake that is interfingered with the Bradbury group sediments. Since then, *Curiosity* has also been analyzing samples from the Stimson formation, an eolian sandstone that unconformably drapes over the Murray mudstone at the base of Mount Sharp. Chapter 5 compares geochemical trends in the Bradbury fluvio-deltaic sediments, the Murray mudstone, and the Stimson eolian sandstone, focusing on our understanding of the source rocks around Gale crater based on clastic input to each of these formations, which sample different areas due to their distinct transport and depositional environments.

Chapter 2

Volumetric Estimates of Ancient Water on Mount Sharp Based on Boxwork Deposits, Gale Crater, Mars

Kirsten L. Siebach and John P. Grotzinger

This chapter is published as:
Siebach, K. L., and J. P. Grotzinger. (2014) Volumetric Estimates of Ancient Water on Mount Sharp Based on Boxwork Deposits, Gale Crater, Mars. *J. Geophys. Res.,* online 28 Jan 2014, doi: 10.1002/2013JE004508.

Key Points

- Boxwork structures on Aeolus Mons (Mount Sharp) are identified and mapped
- Minimum water volume required for boxwork calculated from water-to-cement ratio
- Implications for Mount Sharp formation are discussed

Abstract

While the presence of water on the surface of early Mars is now well-known, the volume, distribution, duration, and timing of the liquid water have proven difficult to determine. This study makes use of a distinctive boxwork-rich sedimentary layer on Mount Sharp to map fluid-based cementation from orbital imagery and estimate the minimum volume of water present when this sedimentary interval was formed. The boxwork structures on Mount Sharp are decameter-scale light-toned polygonal ridges that are unique compared to previous observations of Martian fractured terrain because they are parallel-sided ridges with dark central linear depressions. This texture and the sedimentary setting strongly imply that the ridges are early diagenetic features formed in the subsurface phreatic groundwater zone. High resolution orbital imagery was used to map the volume of light-toned ridges, indicating that a minimum of $5.25*10^5$ m^3 of cement was deposited within the fractures. Using a brine composition based on observations of other Martian cements and modeling the degree of evaporation, each volume of cement requires 800 – 6700 pore volumes of water, so the mapped boxwork ridge cements require a minimum of 0.43 km^3 of water. This is a significant

amount of groundwater that must have been present at the -3620 m level, 1050 m above the current floor of Gale Crater, providing both a new constraint on the possible origins of Mount Sharp and a possible future science target for the *Curiosity* rover where large volumes of water were present and early mineralization could have preserved a once-habitable environment.

2.1 Introduction

The past decade of rover and orbiter missions make the influence of liquid water on the surface environment of ancient Mars very clear [*Malin and Edgett*, 2003; *Squyres et al.*, 2004; *Bibring et al.*, 2006; *McEwen et al.*, 2007b; *Murchie et al.*, 2009]. However, the volume of water that was once available on the surface of Mars, and which likely was subsequently lost to space [e.g. *Jakosky*, 1991], sequestered as ice caps and frozen grounds [e.g. *Plaut et al.*, 2007], or incorporated in rocks and minerals [e.g. *Mustard et al.*, 2012], etc., is much debated. An early estimate that attempted to approximate the surface water inventory based on the cumulative volume of sediment excavated by the numerous outflow channels and valley networks on Mars indicated that a minimum 500 m global equivalent layer (GEL) of water must have been present on early Mars [*Carr*, 1987]. Other estimates have considered the volume of water needed to fill the northern ocean (100 m GEL) [e.g. *Head et al.*, 1999], the amount of water integrated into hydrated minerals (150-1800 m GEL) [*Mustard et al.*, 2012], or the total amount of hydrogen lost to space (95-99% of initial inventory) [*Jakosky*, 1991]. These large-scale estimates serve as a starting point for more specific discussion of local phenomena that may have contributed to regional water budgets.

Recent approaches to quantifying past water abundances exploit the increased resolution of recent orbiter missions to focus, for example, on well-defined geomorphic features that permit better constraints and allow modeling of the minimum water volumes required to form those features, including channels [e.g. *Baker and Milton*, 1974; *Burr et al.*, 2009], basins [e.g. *Goldspiel and Squyres*, 1991; *Jerolmack and Mohrig*, 2007], and alluvial fans or deltas [e.g. *Di Achille and Hynek*, 2010]. These smaller-scale, better constrained, conservative calculations are particularly useful when coupled with

mineralogic evidence for water or when they provide context for larger sedimentary or geologic structures [e.g. *Jerolmack et al.*, 2004; *DiBiase et al.*, 2013] et al. Here, we evaluate a site where groundwater flowed through fractured rock and precipitated cements that formed large-scale boxwork structures. These structures enable estimation of water volumes required to form a specific interval of the sedimentary layers that comprise Aeolus Mons (informally known as Mount Sharp) in Gale Crater. The calculation of water volume at this height, many hundreds of meters above the current crater floor, places important constraints on processes occurring during diagenetic modification of Aeolus Mons. Furthermore, this site is characterized by a once water-rich environment that underwent early mineralization, which is known on Earth to help facilitate preservation of once-habitable environments [*Grotzinger et al.*, 2012]. This is therefore recommended as a priority target for the *Curiosity* rover that successfully landed at the base of Mount Sharp in August 2012.

2.2 Boxwork Structures: Mapping observations and formation discussion

2.2.1 Methodology

Mapping of the boxwork texture was accomplished using orbital imagery available through the NASA Planetary Data System. The gridded topographic dataset (463 m/pixel) from the Mars Orbiter Laser Altimeter (MOLA) instrument onboard the Mars Global Surveyor [*Smith et al.*, 2003] was used as a reference for correlating orbital data over the fractures. Thermal Emission Imaging System (THEMIS) global IR daytime imagery (232 m/pixel) was correlated to the MOLA reference, Context Camera (CTX) images (6 m/pixel) were correlated to the THEMIS reference, and finally High Resolution Imaging Science Experiment (HiRISE) imagery (25 cm/pixel) was correlated to the CTX images. The fracture networks were identified in the HiRISE images and exposures of the fractures were mapped over approximately 1 km^2.

HiRISE Digital Terrain Models (DTMs, 1 m/pixel) provided by the U. S. Geological Survey (USGS) [*Mattson et al.*, 2011] were co-registered where available to determine fracture elevations and stratigraphic relationships. The USGS creates DTMs based on the method described in [*Kirk et al.*, 2008]. The absolute elevations of these

DTMs is determined by comparison to MOLA elevations, and is accurate to within a few tens of meters, but the expected vertical precision (EP) within the DTM can be calculated based on the viewing geometry and resolution of the HiRISE image [*Kirk et al.*, 2008]. For the two DTMs used in this study, the EP, assuming 0.2-pixel matching error, is 7 cm for DTEEC_001488_1750_001752_1750_U02 and 15 cm for DTEEC_019698_1750_019988_1750_U01. Relative elevations within the fractured bed were determined using the HiRISE DTMs, and absolute elevations to compare with the landing site were determined by comparing averaged HiRISE DTM and MOLA gridded values over the mapped fracture networks to the MOLA-based landing site elevation. Fractures were mapped to the limit of resolution of HiRISE 25-cm-pixels, so ridges were detectable if they were about 50 cm across, and their heights could be measured to within about 10 cm based on DTM resolution.

2.2.2 Observations

Resistant fracture networks (boxwork textures) on Mount Sharp were first identified during Mars Science Laboratory (MSL) landing site assessment [*Thomson and Bridges*, 2008; *Thomson et al.*, 2011]. Anderson and Bell placed the fractures in the context of geomorphologic units based on HiRISE mapping, noting that the best-developed cemented fractures are in a dark-toned layered unit [*Anderson and Bell*, 2010]. Stratigraphically, these cemented fracture exposures are found in the upper member of the lower formation of the mound strata (Figure 2.1), which exhibits a spectral signature dominated by sulfates [*Milliken et al.*, 2010] and has a thermal inertia of 260 to 420 $Jm^{-2}K^{-1}s^{-1/2}$ [*Fergason et al.*, 2012].

Mapping of the boxwork texture in this study revealed that it is exposed in a stratigraphic interval at an average elevation of -3620 +/- 50 m with reference to the geoid. This interval is approximately 880 m above the Bradbury Rise landing site for MSL *Curiosity* [*Parker et al.*, 2013], and 1050 m above the current base-level in Gale Crater [*Anderson and Bell*, 2010]. The upper limit of boxwork-containing strata is sharply bounded and coincides with a bedding plane. The interval is abruptly overlain by light-toned strata that lack the boxwork texture. In contrast, the lower boundary of boxwork-

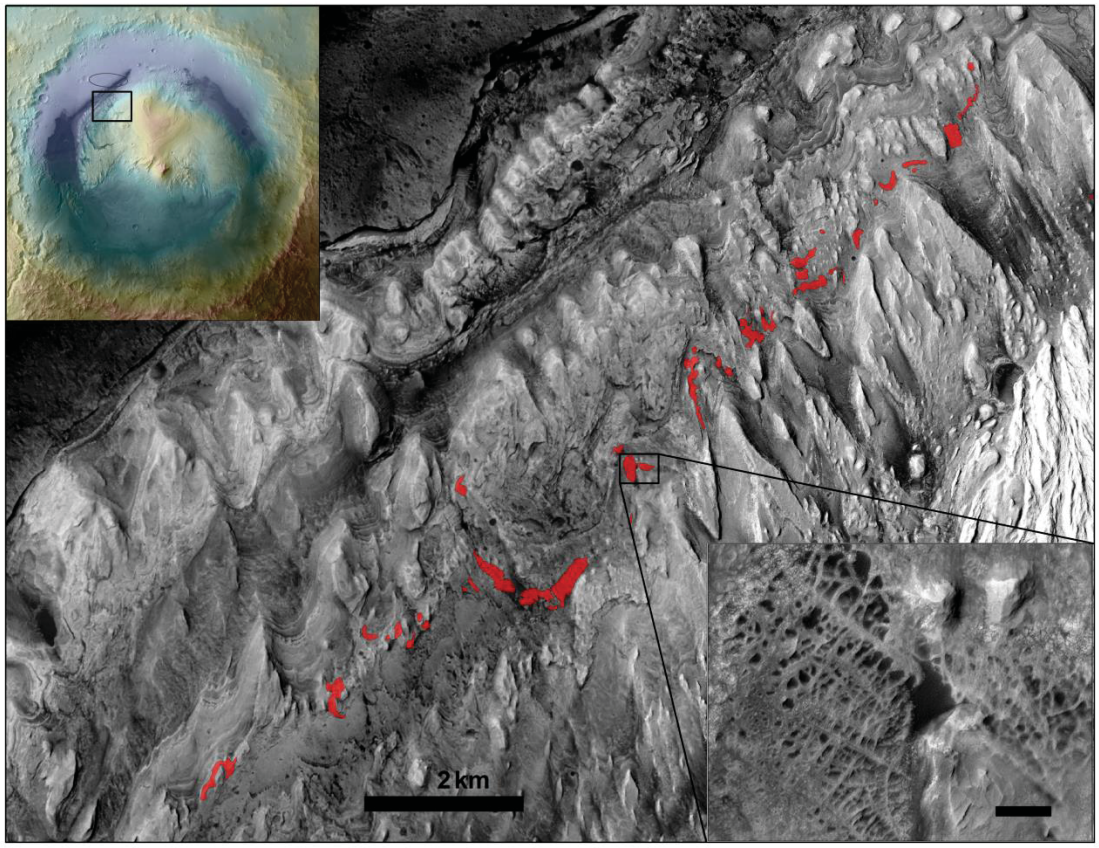

Figure 2.1 Overhead Map of Boxwork Structures
Map of the mapped boxwork structures (red) within the Gale Crater stratigraphy on CTX mosaic with 2 km scale bar. Upper left map of Gale crater shows High Resolution Stereo Camera imagery draped on MOLA topography. Gale crater is 155 km in diameter for scale. Lower right inset shows detail of boxwork structures with a 50 m scale bar. HiRISE images used for mapping include: ESP_012551_1750, ESP_019698_1750, and (inset) PSP_001752_1750. Images centered at 137.302088° E, 4.875233° S.

containing strata is diffuse; boxwork textures gradually dissipate downward through ~40 m of strata as measured in two visible sections in HiRISE DTMs (e.g. Figure 2.2e). Although exposure is intermittent, the boxwork texture can be traced through more resistant intervals. The boxwork-bearing unit is primarily exposed along cliff faces and in open-ended topographic lows between resistant outcrops of the capping unit (Figure 2.3). The light-toned ridges that help define well-developed boxwork textures are fairly densely spaced; these ridges make up an average of 35% of the surface area in these sections (ranging from ~20-50%, Figure 2.2a-d).

The geometry of the fracture network that defines the boxwork texture is delineated by the trends of light-toned ridges, expressed in raised relief. Fractures are mostly straight, however the longest fractures often show slight curvature (e.g. Figure 2.2a-d). The fractures tend to intersect at 90-degree angles and show a preferred orientation; secondary fractures often end when they intersect primary fractures, although secondary fractures may cross-cut primary fractures. The fracture networks are less well-organized at deeper stratigraphic levels, showing increasing fracture curvature and greater intersection angles (Figure 2.2e-f). Ridge widths vary between exposures, but they average about 5 m in width. Some light-toned ridges show a dark line running down the center of the ridge, which varies in width up to 1.5 m (Figure 2.4).

The hollows between elevated boxwork-defining fractures are filled with dark sediment that forms dunes in larger accumulations. These hollows tend to be quasi-circular in plan-view and range in diameter from tens of meters to below one meter, with an average of ~10 m. HiRISE DTMs were used to measure the elevation difference between ridge tops and the middle of the hollows. In many cases the hollows were quite shallow or filled with sand and there was not a measureable difference in elevation. For 25 profiles where there was a measureable difference in elevation, the average elevation difference was 0.4 m, and the elevation differences typically ranged from 0.1 m to 1.0 m (see Figure 2.4). The maximum elevation difference found was 3.5 m between the ridge and hollow.

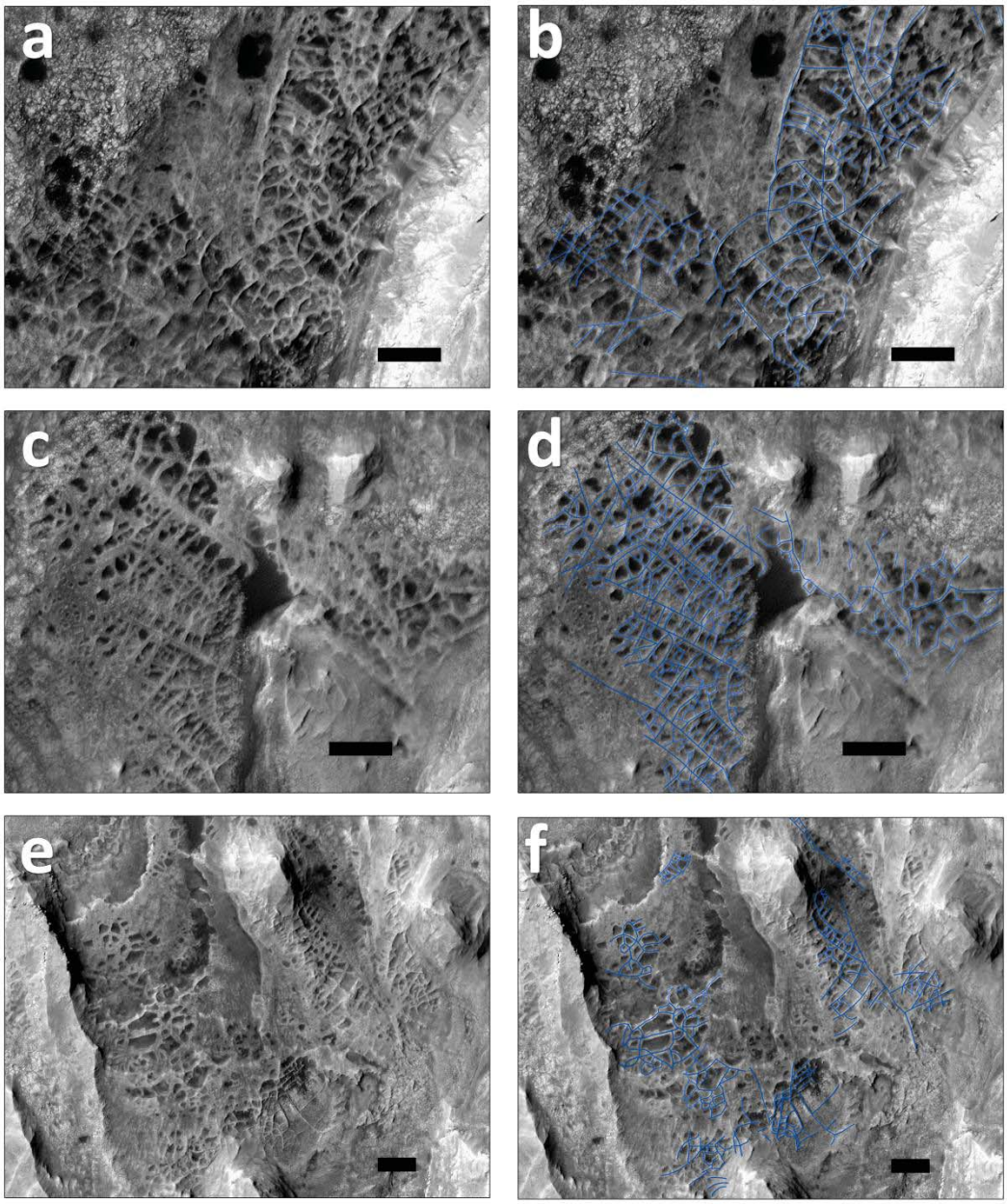

Figure 2.2 Boxwork Structure Morphologies
Images on right (b, d, and f) show outlines tracing the center of the light-toned raised ridges (original fracture network). Scale bar in all images is 50 m, north is up. All images from HiRISE frame PSP_001752_1750. Note clear primary and secondary fracture directions near top of stratigraphic layer (frames c and d) and increasing fracture curvature with depth in the stratigraphy (as shown in a, b, e, and f). Center latitude and longitude of each image pair listed here: (a, b) 137.288197E, -4.900521S, (c, d) 137.302600E, -4.876048S, and (e, f) 137.328993E, -4.845897S.

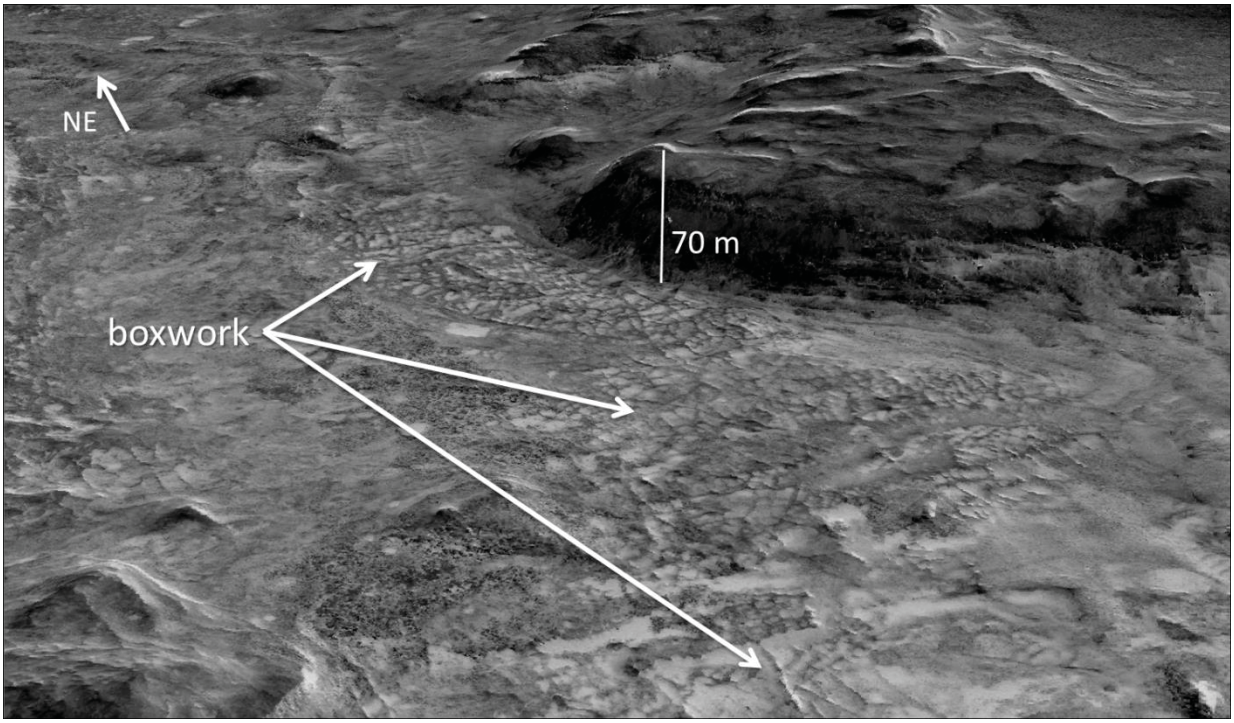

Figure 2.3 Perspective View of Boxwork from HiRISE DTM [DTEEC_001488_1750_001752_1750_U02] of boxwork structures in stratigraphy. Note that the fractures do not continue into the capping unit.

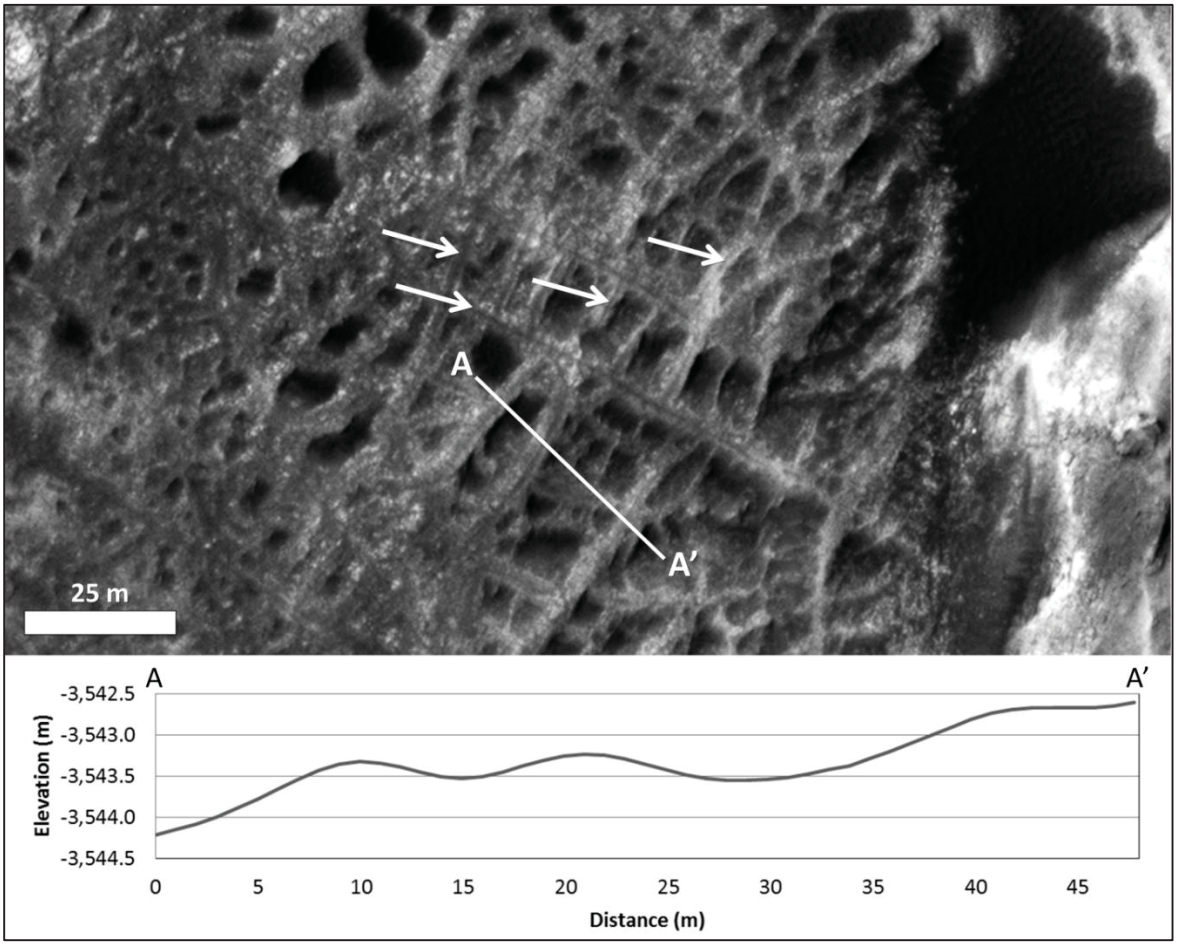

Figure 2.4 Detail of Boxwork Structures
Detail of boxwork structure, showing dark lines in ridge centers. Profile shows that relief between ridges and hollows is on the order of a few tens of centimeters.

2.2.3 Boxwork Formation Discussion

The boxwork texture is defined by light-toned, decameter-scale, polygonal ridge networks. The distinctive attribute of these light-toned ridges as compared to other fracture networks observed from orbit on Mars is that they are parallel-sided with dark center lines that demarcate either linear central depressions or later cements. This texture strongly implies that the ridges are post-depositional diagenetic features formed in the subsurface when mineral-saturated groundwater flowed through fractured, lithified rock, and cement precipitated within fractures and pores. The parallel walls of the filled fractures are comparable to "isopachous" void-filling cements described commonly in rocks on Earth, where minerals create linings, or coatings, along the margins of voids – be they fractures or intergranular pore spaces. Such isopachous cements form when the void is within the phreatic (water-saturated) zone [*Tucker*, 2009]. This differential cementation makes the fractures more resistant to erosion than the less cemented host rock, and thus the fracture fills stand as topographically higher rims around the eroded host rock (Figure 2.1).

Boxwork formation implies a series of post-depositional processes: sediment was lithified and fractured, then saturated fluids percolated through the fracture network and cemented fractures and residual pore spaces in the subsurface, finally the boxwork interval was exhumed and erosion of the less-indurated rock formed the now exposed polygonal ridges. These observations help to clarify the series of events at this stratigraphic interval on Mount Sharp.

The presence of fractures in a distinct stractigraphic successsion, with increasing organization towards the top of that succession, and the absence of similar fractures in overlying strata imply that this stratum was already lithified and then exposed at the surface when the fracturing occurred. Lithification on Mars is not well understood, but in general, compaction by burial decreases porosity of sediments and fluids cement and lithify sediments [*Grotzinger and Milliken*, 2012]. Conceivably, this boxwork-bearing interval could have been buried, infiltrated by cementing fluids, and converted from sediment to rock, prior to exhumation and fracturing.

The fracture geometry helps narrow down the cause of fracturing. In general, large non-tectonic surface fractures originate from contraction, impact processes, loading and

unloading of lithospheric stresses, jointing, or fluid pressure [*Long et al.*, 1996]. Jointing and fluid pressure are ruled out by stratigraphic relationships—the fracturing occurred at the surface—and impact processes are ruled out by the systematic organization of fractures (Figure 2.2). Contraction processes are the most likely to have formed the fractures. The observed orthogonal fracture patterns indicate that the fractures did not form in extended freeze/thaw cycles, which create 120-degree joints over 10^6-year time scales [*Sletten et al.*, 2003]. Rather, the fracture geometry is most similar to those formed in non-cyclic isotropic or slightly non-isotropic contraction stress fields [*Olson et al.*, 2009], which could be related to sediment desiccation or more intense short-term freezing of lithified sediment [*Long et al.*, 1996].

After lithification and fracturing, the voids in the host rock and fractures are inferred to have been filled with a second generation of cement. The dark line in the center of the ridges helps delineate the parallel-sided or "isopachous" nature of precipitated fracture-filling minerals along the walls of the fractures (e.g. Figure 2.4). The isopachous morphology of the light-toned elevated ridges is consistent with cementation in the phreatic groundwater zone, where cement formation occurs evenly on all available surfaces.

Approximations of the water volume required to form the ridges depend on the relative proportion of primary host rock, and secondary cements forming the raised ridges. Two scenarios are proposed for the relative proportions of primary rock and secondary cement in the light-toned ridges: (1) the ridges are primarily composed of extensive secondary cements filling pores and fractures, or (2) the ridges are mostly composed of the host rock, hardened by an early cement within the pore spaces. For either case, there are then two options for the dark central lineations in the ridges; the dark lines could represent residual porosity in the fracture network that was back-filled with wind-blown dark sand or dark-toned cement that completely fills the fracture void. Since the dark central lines are a relatively minor component of the ridges, the primary distinction between these scenarios is whether the light-toned ridges are mostly cement or if they are host rock with pore-occluding cement, perhaps ~30% cement fill. Orbital data cannot discriminate between these two scenarios. However, in either case, the observed boxwork represents a significant volume of cement precipitated from groundwater.

Polygonal ridges, albeit at a much smaller scale, were originally analyzed and described in Wind Caves, South Dakota, where the term "boxwork" structures was coined [*Bakalowicz et al.*, 1987]. Large-scale intersecting filled fracture networks are also present in sulfate-bearing units in Candor Chasma [*Okubo and McEwen*, 2007] and northeast Syrtis Major [*Ehlmann and Mustard*, 2012], but the structures within Mount Sharp are distinguished as a dense, parallel-sided network of filled-fracture boxwork structures.

Alternative formation hypotheses for the boxwork were considered, but they do not explain the observed fracture characteristics and the dark line in the center of the ridges. Volcanic dikes, for example, could also leave raised ridges post-erosion, but these often form in clusters or irregular parallel geometries [*Hoek*, 1991], and this formation mechanism does not explain the centered dark lines. Some freeze-thaw thermal contraction polygons have dark central lines that demarcate accumulations of loose sediments between ice polygons, and the edges of the ice polygons may accumulate raised shoulders, but the central linear depressions (sand wedges) are generally wider than the raised polygon shoulders [*Sletten et al.*, 2003]; this does not match the measured elevated ridges described here. Finally, boxwork patterns could be similar to large-scale honeycomb or tafoni salt-weathering patterns [*Rodriguez-Navarro*, 1998], but this is unlikely because of the high ridge width relative to hollows and the albedo variation in the ridges. Based on the fracture geometry, presence of sulfates, ridge characteristics, and local geomorphic features consistent with water-induced bedrock erosion [*Anderson and Bell*, 2010], the cementation-based hypothesis for boxwork formation is accepted as the most likely interpretation.

2.3 Fluid Volume Calculation

Quantitative estimates of water flow on Mars are essential to understanding water-rock interactions that inform an understanding of diagenesis and alteration, as well as habitability. At Gale Crater, these estimates would help provide context for *Curiosity's* mission of exploration. The boxwork structures described here constitute an unusual opportunity where quantitative measurements of a volume of diagenetic cements can be acquired from orbital imagery. Cement volumes can be related to the volume of water

required to deposit the cement if a few simple assumptions are made about the ion saturation of the groundwater and the degree of evaporation of the brine. An approach to fluid pore-volume calculations based on terrestrial studies of carbonate cementation is employed here to determine the water volume required to deposit the mapped cements [*Bethke*, 1985; *Banner and Hanson*, 1990]. Although the cement composition of the ridges was not uniquely determined from orbit, previous observations of evaporite deposits on Mars by the *Opportunity* rover [*Grotzinger et al.*, 2005; *McLennan et al.*, 2005] have constrained models of Martian brines. Here we use an evaporation model derived from acid-sulfate weathering of synthetic Martian basalts and constrained by the *Opportunity* rover findings in Meridiani Planum [*Tosca*, 2004; *Tosca et al.*, 2008].

Calculation of the minimum volume of water required to form the boxwork layer is based on the following equation:

$$\frac{V_{water}}{V_{cement}} = \left[\sum_{minerals} \left(\frac{m_{mineral}}{V_{brine} * \rho_{mineral}} \right) \right]^{-1}, \qquad (1)$$

where the volume of cement (V_{cement}) is derived from mapping of orbital imagery and the minerals precipitated are derived based on a reasonable model for evaporation of a Martian brine [*Tosca et al.*, 2008]. The volume of water (V_{water}) evaporated per volume of cement precipitated (V_{cement}), or unitless "pore volume," is calculated for a given degree of brine evaporation based on the volume of precipitated minerals ($m_{mineral}/\rho_{mineral}$) per volume of water in the initial brine (V_{brine}). The results of this calculation are shown in in Figure 2.5, where pore volumes of water (V_{water}/V_{cement}) are plotted against percent of water evaporated (V_{water}/V_{brine}). The plot seems to approach an asymptote, indicating that more water evaporation does not immediately lead to more cement precipitation, at two times; first after the precipitation of jarosite, gypsum, copiapite, and bilinite, and later after the precipitation of epsomite, melanterite, anhydrite, and halite [*Tosca et al.*, 2008]. Points near the two asymptotes are selected to describe the range of pore volumes of water that would be required to deposit the cement volume. As indicated in Figure 2.5, if 99% of the starting brine evaporates, then 6,700 pore volumes of water are required, or (based on the last point in the modeled evaporation sequence) if 99.97% of the brine evaporates, 800

pore volumes of water are required to form the cements. These values fit well in the range of pore volumes estimated for terrestrial porosity occlusion scenarios [*Bethke*, 1985; *Banner and Hanson*, 1990].

To obtain a minimum estimate for the water volume, the volume of cement is derived from the surface area of ridges within the mapped HiRISE unit, 0.35 km^2, multiplied by the thickness of the resistant boxwork layers in the vertical stratigraphy, 5 m, giving a minimum cemented ridge volume of 1.75 x 10^6 m^3. This is a conservative estimate as the boxwork can be traced vertically through up to 40 m of stratigraphy in some locations and may well extend laterally for some distance into the subsurface beneath Mount Sharp, based on continuity of stratigraphy around the entire mound [*Milliken et al.*, 2010]. Two endmember hypotheses were used to calculate the cement volume based on the ridge volume: ridges are 100% cement (cements occur within fractures), or ridges are 30% cement by volume (cements occlude pores within primary rocks adjacent to fractures). The pore-occluding scenario is comparable to several analogous locations on Earth, where rocks in close proximity to a fracture or fault can become strongly cemented, forming diagenetic "halos" [*Knipe*, 1992; *Nelson et al.*, 1999]. Assuming 99.97% of the brine evaporates, the fracture-filling scenario requires a minimum of 1.4 km^3 of water, and the pore-occluding scenario requires 0.42 km^3 of water to form the measured ridges (Figure 2.5).

2.4 Implications for Mount Sharp Formation

These results are surprising because they imply a significant amount of water once percolated through pores in rocks 1050 m above the current base-level for Gale Crater. Several scenarios could deliver the required water, but this analysis must begin with several firm constraints: (1) the boxwork fabric is developed along a bedding plane that emerges from within the stack of layers that define Mt. Sharp, (2) the boxwork fabric terminates abruptly against the overlying stratum, but extends downward for several tens of meters, and (3) the isopachous element of the boxwork fabric indicates mineral precipitation in the phreatic zone, below the local groundwater table. These constraints require the boxwork to be an ancient feature, dating back to the time of sediment accumulation; development of

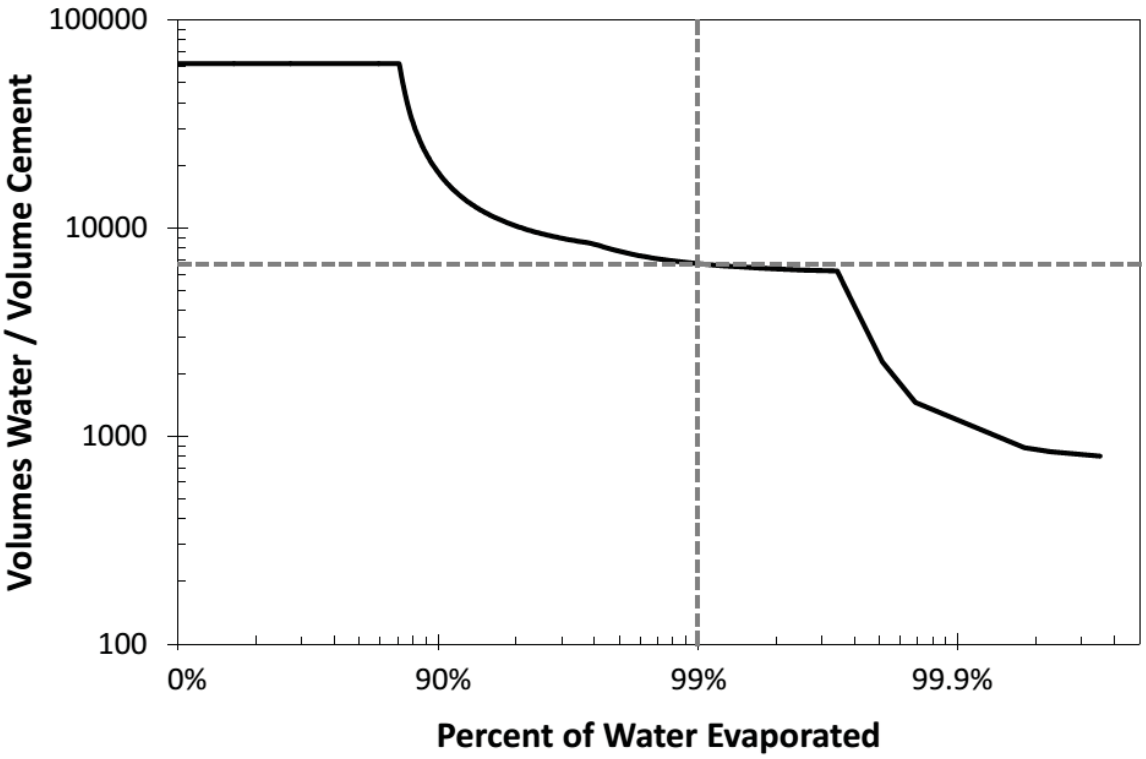

Figure 2.5 Plot of Required Volumes of Water per Volume Cement
Plot showing unit volumes of water evaporated per unit volume of cement precipitated (pore volumes of water) depending on the percent of water evaporated from a Martian brine model based on findings from the Mars Exploration Rover Opportunity [*Tosca et al.*, 2008]. The plot approaches an asymptote, indicating that more water evaporation does not immediately lead to more cement precipitation, twice; first after the precipitation of jarosite, gypsum, copiapite, and bilinite, and later after the precipitation of epsomite, melanterite, anhydrite, and halite [*Tosca et al.*, 2008]. Dotted line shows that if 99% of the brine evaporates, 6,700 pore volumes of water are required per unit of cement deposited. At the last point in the model, when 99.97% of the water has evaporated, only 800 equivalent volumes of water are required per volume of cement.

the fractures was terminated before the time of deposition of the overlying stratum; mineral precipitation occurred in the fractures in the phreatic zone, below the local groundwater table. This volume of groundwater-based cement indicates that the mound was formed not simply by eolian sediments cemented in minor wetting events [e.g. *Kite et al.*, 2013] but that instead there was extensive groundwater flow and aqueous processing of sediments involved in mound formation (see Figure 2.6).

Perhaps the simplest explanation is that the boxwork texture reflects groundwater supplied by atmospheric precipitation either as rain or snow; basin-filling strata accumulating within the lower elevations of Gale crater could have absorbed water in this fashion. The waxing and waning of water derived from seasonal or longer-term climatic cycles could have provided a mechanism for fracture formation [*Lachenbruch*, 1963]. However, this mechanism cannot account for the mineral abundance required to create the fracture-filling cements. Meteoric waters derived from rainfall or melting snow on the -3620 meter bedding plane surface would have been strongly undersaturated and almost certainly would have resulted in dissolution and karst formation given the high solubility of sulfate salts. In contrast, the evidence presented in this paper strongly supports mineral precipitation at this stratigraphic level. There is no evidence for dissolution fabrics which have been detected elsewhere based on remotely-sensed image data [*Belderson et al.*, 1978; *Manda and Gross*, 2006].

A derivative scenario assumes that Mt. Sharp had topographic expression at the time the boxwork-containing strata were accumulating and that precipitation occurred in those highlands. The recharge area underwent leaching to provide the ions required to cause mineral precipitation at some down-gradient distant site – for example, where the boxwork fabric is observed (Figure 2.6a-b). Mt. Sharp has considerable surface area and, depending on the mechanism for its formation, it is conceivable that its summit varied in position; the current summit is about 45 km southeast from the exposed boxwork bedding plane. The stratigraphic interval represented by the fracture network would have been within an aquifer, transporting these fluids down-gradient from the undersaturated recharge area. As fluids moved through this aquifer they would have become increasingly saturated due to dissolution of minerals along the way, and eventually re-precipitated these dissolved

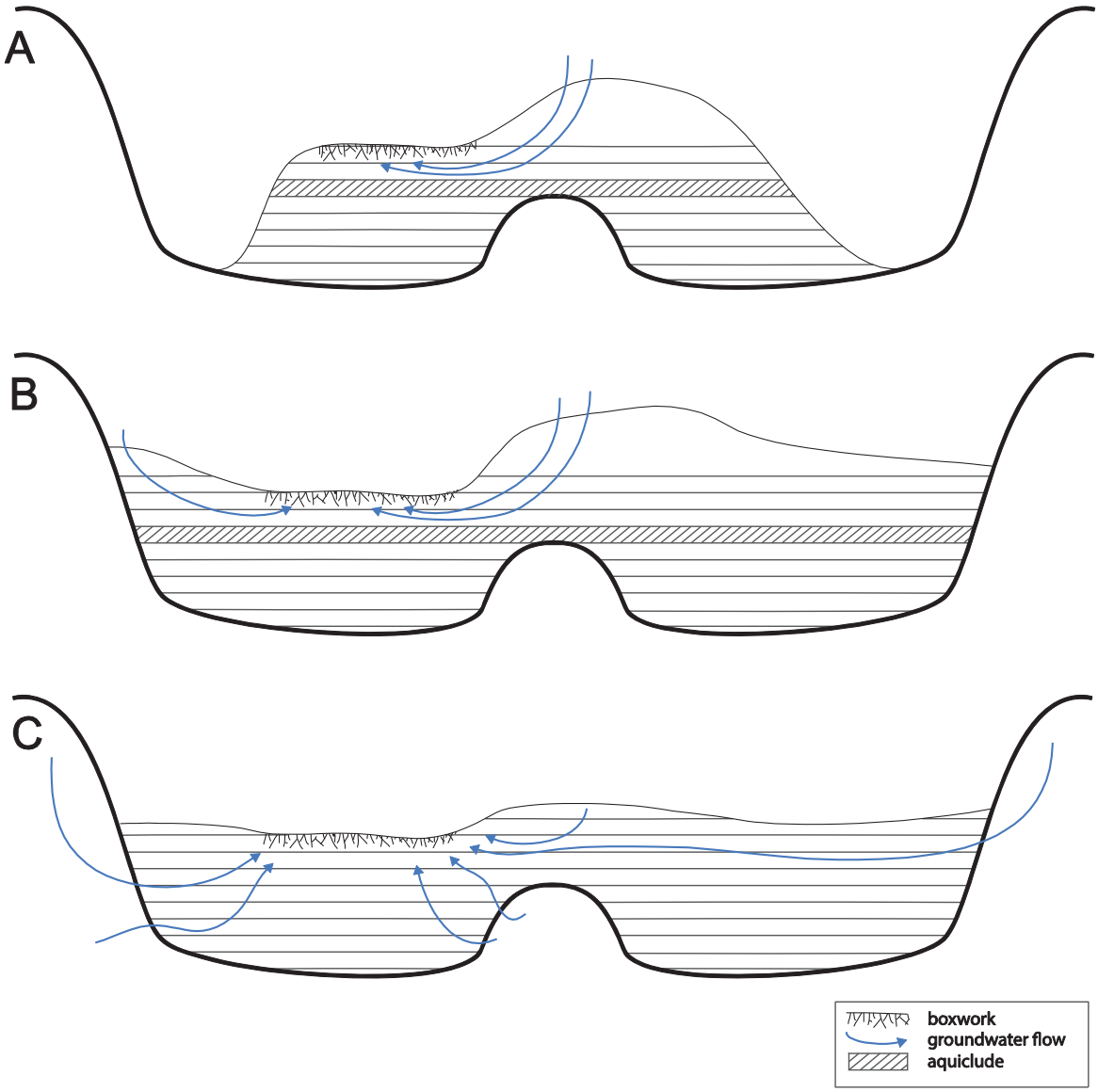

Figure 2.6 Schematic of Mount Sharp Formation Models
Schematic showing possible ancient configurations of Mount Sharp that would allow sufficient groundwater flow to form boxwork structures. Part a shows a scenario where Mount Sharp formed as a central mound with an aquiclude, where groundwater must have originated from precipitation on topographically high parts of the mound, and evaporated in locations with low overburden pressure, forming the boxwork structures. Part b shows a scenario where most of the crater is filled with sediments and the boxwork form in a topographic low because an aquiclude prevents groundwater from sinking in the crater. Part c shows a less conservative scenario where the crater is full of sediments and focuses groundwater from the surrounding region that evaporates to form the boxwork.

ions where physical conditions caused local oversaturation. (A variety of soluble minerals might have been involved in dissolution updip, to precipitation downdip, but such considerations go beyond the scope of the current paper.) This mechanism would have required Mt. Sharp to have a higher elevation than the -3620 m bedding plane to drive the flow. It also likely would have required a perched water table (unless the whole mountain was saturated), underlain by an aquiclude, to prevent infiltration and loss of the fluid at sites far removed from the recharge area. It is conceivable that in the Mt. Sharp stratigraphy there exist lithologies heterogeneous enough to provide contrasts in hydraulic conductivity. This scenario allows for the possibility, but does not require, that Gale Crater was mostly filled with sediment (Figure 2.6b); as long as the aquifer including the boxwork has sufficient topography and area to serve as a recharge area for the groundwater flow, the sediment need not have filled the entire crater (Figure 2.6a).

A less conservative but viable scenario would invoke filling of Gale Crater with sediments up to the level of the -3620 m bedding plane (Figure 2.6c) [*Malin and Edgett*, 2000]. These sediments could have lithified and fractured based on sediment water flux or thermal expansion-contraction. Subsequent burial due to continued sediment accumulation could have resulted in circulation of mineral-saturated groundwaters in the fracture network, with later precipitation of minerals in the fractures. Eventually, these strata were exhumed, creating Mt. Sharp and exposing the bedding plane on which the boxwork fabric is developed.

2.5 Conclusions

Detailed mapping of the filled fracture network on Mount Sharp indicates that this sedimentary layer most likely represents large-scale boxwork fabrics. The original sedimentary rock was lithified, likely by early cementing fluids during shallow burial. Subsequently this layered unit was exposed at the surface and fractured, and then it was again buried. Circulation of mineral-saturated fluids in the phreatic zone further lithified sediments adjacent to the fractures and also at least partially filled the fractures. This sequence of events requires circulation of mineral-saturated groundwater, supporting mound-formation scenarios in which groundwater could migrate from an undersaturated

recharge area to precipitate within the boxwork level at least a kilometer above the current crater floor.

Volumes of diagenetic cements can be measured from orbital imagery and, based on these measurements and an assumed chemistry, the minimum volume of water required to form the cements measured was calculated to be about 0.4 km^3. These deposits provide evidence for extensive and relatively rapid cement formation, which could be beneficial to the preservation of organic compounds, 1050 m above the current floor of Gale Crater.

The Mars Science Laboratory *Curiosity* rover is capable of driving to the boxwork layer [*Grotzinger et al.*, 2012] from its landing site on the floor of Gale Crater and investigating the chemical composition and textures of these deposits from the surface. This site is a possible target for investigation by *Curiosity* as a location where a series of post-depositional water-based processes are interpreted that left extensive exposed diagenetic cements, which are indicative of possibly favorable conditions for preservation of organic compounds.

Acknowledgements

This work was supported by the Caltech GPS fellowship fund and a NASA Astrobiology Institute grant #NNA13AA90A to JPG. We thank K. Stack for help determining the DTM precision, N. Tosca for providing brine evaporation results, and Mars Science Laboratory science team colleagues for helpful discussions. Helpful reviews by M. Ramy El-Maarry and R. Irwin improved this manuscript.

Chapter 3

Subaqueous Shrinkage Cracks in the Sheepbed Mudstone: Implications for Early Fluid Diagenesis, Gale Crater, Mars

Kirsten L. Siebach, John P. Grotzinger, Linda C. Kah, Kathryn M. Stack, Michael Malin, Richard Léveillé, and Dawn Y. Sumner

Chapter 3 is published in:
Siebach, K. L., J. P. Grotzinger, L. C. Kah, K. M. Stack, M. Malin, R. Leveille, and D. Y. Sumner. (2014) Subaqueous Shrinkage Cracks in the Sheepbed Mudstone: Implications for Early Fluid Diagenesis, Gale Crater, Mars. *J. Geophys. Res.*, online 17 Jul 2014, doi: 10.1002/2014JE004623.

Key Points

- Raised ridges are early diagenetic cement-filled cracks in Sheepbed mudstone
- Cracks are subaqueous shrinkage cracks likely formed by subsurface gas
- Isopachous cement fills indicate series of pore fluid chemistries

Abstract

The Sheepbed mudstone, Yellowknife Bay formation, Gale crater, represents an ancient lakebed now exhumed and exposed on the Martian surface. The mudstone has four diagenetic textures, including a suite of early diagenetic nodules, hollow nodules, and raised ridges, and later diagenetic light-toned veins that cross-cut those features. In this study, we describe the distribution and characteristics of the raised ridges, a network of short spindle-shaped cracks that cross-cut bedding, do not form polygonal networks, and contain two to four layers of isopachous, erosion-resistant cement. The cracks have a clustered distribution within the Sheepbed member and transition laterally into concentrations of nodules and hollow nodules, suggesting that these features formed penecontemporaneously. Because of the erosion-resistant nature of the crack fills, their three-dimensional structure can be observed. Cracks that transition from sub-vertical to sub-horizontal orientations suggest that the cracks formed within the sediment rather than at the surface. This observation and comparison to terrestrial analogs indicate that these are synaeresis cracks - cracks that formed

subaqueously. Synaeresis cracks form by salinity changes that cause sediment contraction, mechanical shaking of sediment, or gas production within the sediment. Examination of diagenetic features within the Sheepbed mudstone favors a gas production mechanism, which has been shown to create a variety of diagenetic morphologies comparable to the raised ridges and hollow nodules. The crack morphology and the isopachous, layered cement fill show that the cracks were filled in the phreatic zone and that the Sheepbed mudstone remained fluid-saturated after deposition and through early burial and lithification.

3.1 Introduction

Whereas Mars was once considered to be a mostly volcanic planet, the last ten years of exploration have shown that there are a significant number of sedimentary deposits on Mars, and that these rocks record a complex history of water-rock interaction [*McLennan and Grotzinger*, 2008a; *Grotzinger and Milliken*, 2012]. Orbitally-based observations have shown that these rocks form in a range of depositional environments and show a wide variety of spectral signatures [e.g. *Ehlmann et al.*, 2008a; *McLennan*, 2012]. More detailed investigations into sedimentary clast origins, depositional textures, rock lithification, and later rock modifications must be completed at the rover-scale. Diagenesis, in particular, includes all processes that occur after initial sediment deposition and prior to weathering and erosion of an exhumed rock, including the lithification of sediments into rock. Investigation into the diagenetic stages that sediments have undergone helps constrain the duration, continuity, and chemistry of different stages of water-rock interaction. Diagenesis of sediments usually encompasses loss of porosity due to grain reorganization, compaction, and cementation of the rock, and may also include authigenic mineral precipitation, void formation, and sediment deformation [*Worden and Burley*, 2003]. Later diagenetic affects may also include events related to creation of new pore networks, often associated with fracturing and subsequent fluid migration events [*Long et al.*, 1996]. Detailed studies of mineralogy, chemical variability, and textural features can aid in reconstruction of these diagenetic events. Ultimately, understanding diagenetic histories can provide critical constraints on the reconstruction of ancient depositional environments, and the chemical evolution of sedimentary pore fluids.

Effects of sediment diagenesis have been observed on Mars at both rover [*Clark et al.*, 2005; *McLennan et al.*, 2005] and orbiter scales [*Okubo and McEwen*, 2007; *Ehlmann et al.*, 2011; *Siebach and Grotzinger*, 2014a] and have been attributed to the circulation of liquid water through pore networks. In some cases, these observations provide plausible constraints on the volume of water required to form diagenetic signals (e.g. [*McLennan et al.*, 2005; *Siebach and Grotzinger*, 2014a]). At present, most of the diagenetic processes observed by landed missions on Mars, like the sulfate cementation at Meridiani Planum, have pointed to acidic, highly saline groundwaters with low water activity [*Grotzinger et al.*, 2005; *McLennan et al.*, 2005; *Knoll and Grotzinger*, 2006; *Tosca et al.*, 2008], however these compositions may be inherently biased due to the small number of landed missions. More recent findings from the Mars Exploration Rover and Mars Science Laboratory (MSL) missions have shown that more neutral-pH environments, with lower salinity and elevated water activity, were also present on early Mars [*Arvidson et al.*, 2014; *McLennan et al.*, 2014; *Vaniman et al.*, 2014], and that these were potentially habitable environments that could have been suitable for chemolithoautotrophic microbes [*Grotzinger et al.*, 2014].

Since landing in August 2012, the *Curiosity* rover has identified multiple types of sedimentary rock, ranging from conglomerate [*Williams et al.*, 2013] to sandstone and fine-grained mudstone, each of which provide evidence for diagenesis [*Grotzinger et al.*, 2014]. The Sheepbed mudstone, interpreted to have been deposited in an ancient freshwater lake, has undergone extensive study with the full range of analytical instruments on the *Curiosity* rover [*Grotzinger et al.*, 2014]. The Sheepbed mudstone is uniformly fine-grained (<63 μm grain sizes), composed of >15% authigenic clay minerals [*McLennan et al.*, 2014; *Vaniman et al.*, 2014], and contains at least four distinct diagenetic textures: nodules (spheroidal protrusions with no discernable internal structure), hollow nodules (spheroidal protrusions showing a central void), raised ridges, and a later generation of gypsiferous, mineralized veins [*Grotzinger et al.*, 2014; *Nachon et al.*, 2014; *Stack et al.*, 2014]. Collectively, these features record long-term exposure to water, and reveal a once-habitable environment in Yellowknife Bay, Mars [*Grotzinger et al.*, 2014]. Here, we investigate the importance of the raised ridge features and use their characteristics to show that the Sheepbed mudstone

was most likely deposited subaqueously and had fluid-saturated pore spaces throughout early lithification and cementation of the mudstone.

3.2 Geologic Context

After landing at Bradbury Rise (4.589°N, 137.441°E), Gale crater, Mars, the *Curiosity* rover traversed 445 meters west to the Glenelg region [*Parker et al.*, 2013; *Grotzinger et al.*, 2014]. This region represents the conjunction of three units, defined in orbital images based on geomorphic and thermal inertia attributes, which are located at the distal end of an alluvial fan system [*Grotzinger et al.*, 2014]. One of the units that *Curiosity* investigated in detail was the bright, fractured (BF) unit, characterized by relatively high thermal inertia, exposed light-toned bedrock, and ubiquitous decimeter-scale fractures. An approximately five meter-thick exposure of stratigraphic section of the BF unit occurs at Glenelg and has been described as the Yellowknife Bay formation [*Grotzinger et al.*, 2014]. In ascending order, the latter is subdivided into the Sheepbed, Gillespie Lake, and Glenelg members (Figure 3.1). The uppermost Glenelg member consists of fine- to coarse-grained, locally cross-stratified, basaltic sandstone that is interpreted to reflect fluvial or eolian deposition [*Grotzinger et al.*, 2014]. The Gillespie Lake member, also interpreted as a fluvial deposit, consists of a medium-grained sandstone of basaltic composition. Underlying these two relatively coarse-grained deposits rests the Sheepbed member, a mudstone, also of basaltic composition, that is interpreted to have been deposited in a lacustrine setting [*Grotzinger et al.*, 2014]. The contact of the Sheepbed member with the overlying Gillespie Lake member is sharp, and traceable in orbital imagery.

The stratigraphically lowest unit in the Glenelg region, the Sheepbed member, is exposed in the floor of Yellowknife Bay. Based on *Curiosity*'s observations, it extends across at least the ~60 m traversed within Yellowknife Bay. Given that it can be traced from orbit, and likely closely coincides with the BF unit, the Sheepbed member is inferred to extend laterally at least several hundred more meters to the east and north, and is possibly laterally continuous for hundreds of meters or kilometers beneath the overlying units of the Yellowknife Bay formation [*Grotzinger et al.*, 2014]. The Sheepbed member is the best-characterized member of the Yellowknife Bay formation because two drilled samples, John

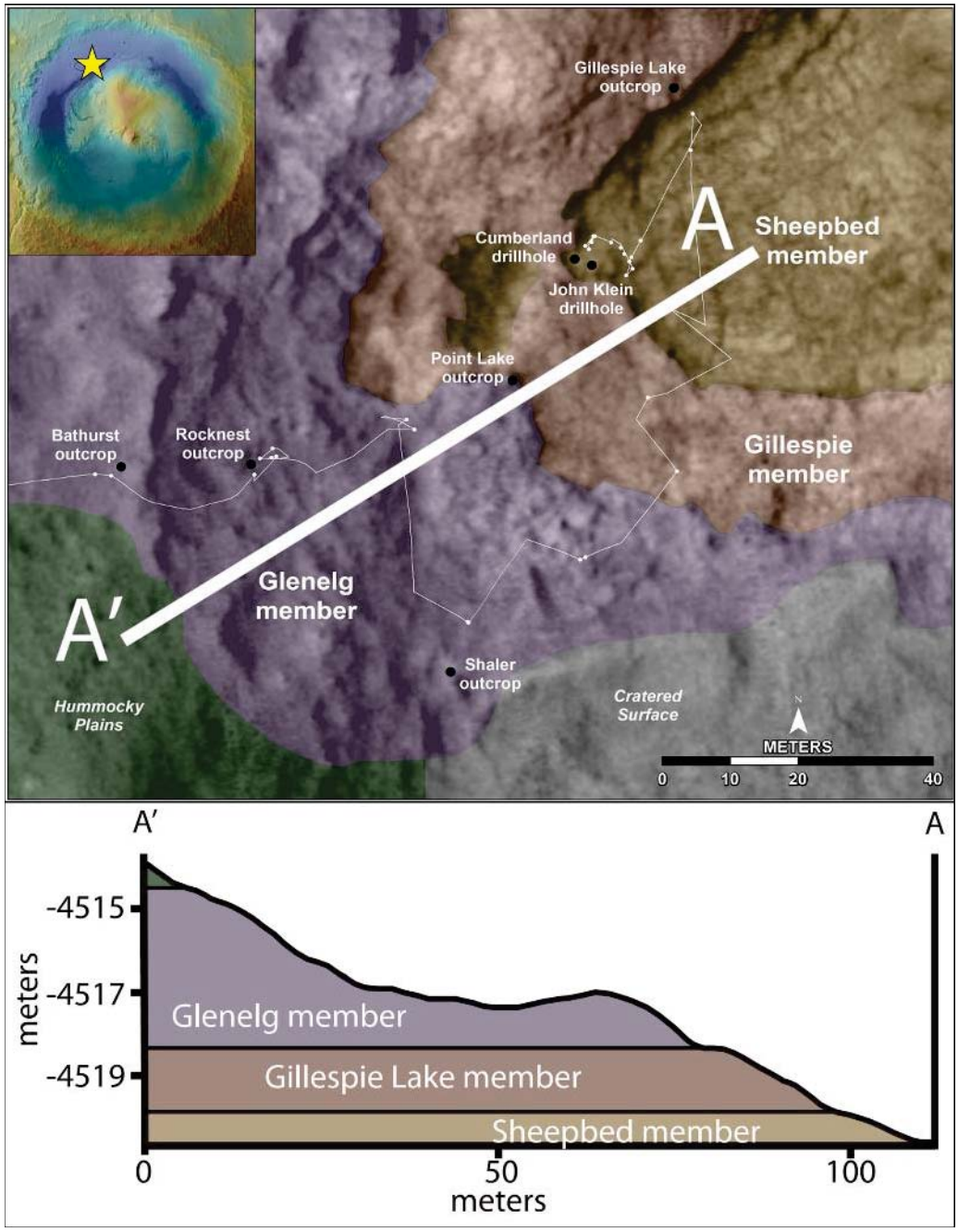

Figure 3.1 Geologic Map of Yellowknife Bay
After *Grotzinger et al.* [2014]. Upper left inset shows Gale crater, 155 km across, with star at Yellowknife Bay location. Lower portion shows members of the Yellowknife Bay formation projected into a HiRISE-extracted elevation profile.

Klein and Cumberland, were acquired from this member and analyzed by *Curiosity's* full analytical instrument suite, including a mass spectrometer and X-Ray Diffraction (XRD) instrument [*Ming et al.*, 2014; *Vaniman et al.*, 2014]. In addition, a suite of Alpha Particle X-Ray Spectrometer (APXS) measurements were collected within the unit [*Grotzinger et al.*, 2014; *McLennan et al.*, 2014] and numerous ChemCam laser-induced breakdown spectroscopy analyses were obtained to help characterize the site [*Léveillé et al.*, 2014; *Nachon et al.*, 2014]. *Curiosity's* investigation demonstrated that the Sheepbed member is uniformly fine-grained, with a near-typical basalt composition, and contains nearly 20% saponitic smectite clay minerals [*Grotzinger et al.*, 2014; *McLennan et al.*, 2014; *Vaniman et al.*, 2014]. The smectite clay, identified by the XRD analysis, was inferred to be authigenic based on the distributed APXS measurements, which showed that the rock chemically matches slightly-alkaline average Martian crustal basalt in all of the samples, suggesting isochemical weathering [*McLennan et al.*, 2014]. Mudstones are generally deposited in low-energy, standing water environments, and the Sheepbed unit, in particular, has been interpreted to have been deposited in a lake that formed at the distal limit of an alluvial fan [*Grotzinger et al.*, 2014].

Diagenetic textures representing at least two distinct post-depositional fluid environments are present in the Sheepbed mudstone. These include nodules, hollow nodules, raised ridges, and light-toned, cross-cutting, calcium sulfate-rich light-toned veins (Figure 3.2) [*Grotzinger et al.*, 2014]. The nodules and hollow nodules are mm-scale resistant spherical protrusions (sometimes with a less-resistant or hollow center) that are densely clustered in some locations [*Stack et al.*, 2014] and pass laterally into concentrations of raised ridges. The light-toned veins weather flush with the surrounding rock and cross-cut the raised ridges, nodules, and hollow nodules (Figure 3.2).

3.3 Methods

Raised ridges—mineralized cracks, only a few mm in width, which are distributed within the Sheepbed member—were mapped over 27 m^2 of the exposed surface of the Sheepbed unit using ArcGIS software and images available through the NASA Planetary Data System. Context for this mapping was derived from High Resolution Imaging Science

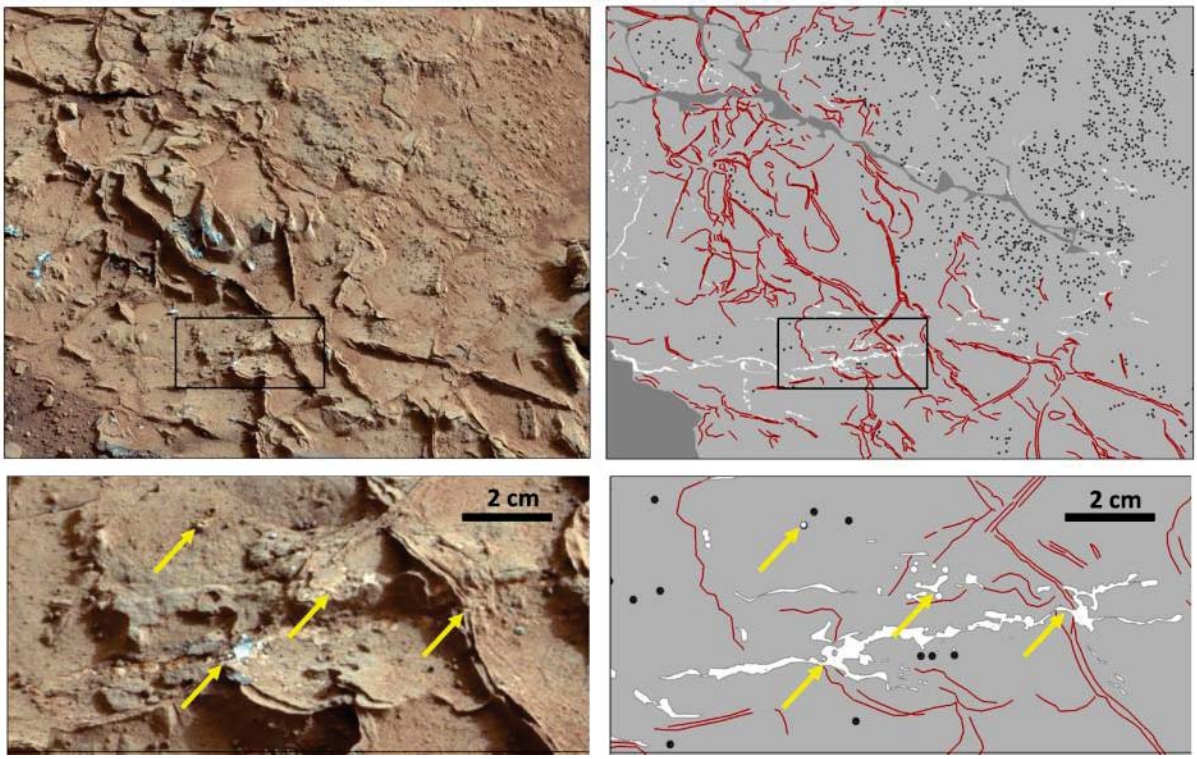

Figure 3.2 Mastcam Image and Interpretation of Raised Ridges
Portions of Mastcam M-100 mosaic (mcam00885, sol 164), with accompanying sketches, showing relationships between diagenetic textures in the Sheepbed unit. Inset box is approximately 13 cm x 6 cm; 2 cm scale bar in inset. Red lines are erosion-resistant cements that compose the raised ridges, dark grey circles are nodules and hollow nodules, white fill shows light-toned veins visible at the surface (many are dust-covered), and dark grey depicts dust covered regions of the mudstone. Yellow arrows in inset highlight cross-cutting relationship showing that the light-toned veins are a later texture that cut through the raised ridges and hollow nodules, sometimes even filling previously-hollow nodules.

Experiment (HiRISE) images (25 cm/pixel) [*McEwen et al.*, 2007a] and orthorectified MSL Navigation Camera (Navcam) imagery [*Maki et al.*, 2012], which have been localized along the rover's traverse by the MSL science team localization scientists based on a controlled photomosaic of sequentially higher resolution data sets tied to the Mars Orbital Laser Altimetry global base map [*Parker et al.*, 2013]. HiRISE imagery was used as a basemap for stratigraphic analysis, and rover-based Navcam imagery was used to create contours and localize ChemCam and drill targets. Neither of these image sets, however, provide adequate resolution to map the raised ridge features.

The *Curiosity* Mast Camera (Mastcam) imagery proved to be the best available imagery to map the sub-mm-scale raised ridge features over a large spatial area (~27 m^2). The Mastcam consists of two mast-mounted cameras that sit approximately 2.1 m above the surface. The right Mastcam (M-100) has a 100-mm focal length, f/10 lens, with a 6.3° x 5.1° field of view (FOV), and the left Mastcam (M-34) has a 34-mm focal length, f/8 lens, with an 18.4° x 15° FOV. The two cameras are separated by a 24.5 cm stereo baseline [*Malin et al.*, 2010; *Bell et al.*, 2013]. Image mosaics taken with the M-100 camera are preferable for mapping the raised ridge features because of their inherent higher image resolution; even for surfaces 5 m away from the rover, the M-100 camera provides a resolution of 0.37 mm/pixel, whereas the M-34 has a resolution of 1.1 mm/pixel. However, because the images are not taken vertically, but at a variable angle, raw M-100 imagery is necessarily distorted relative to the actual topography of the raised ridges. Thus, where available, stereo imagery was used to create orthorectified Mastcam mosaics using the Ames stereo pipeline [*Moratto et al.*, 2010], which was adapted by Malin Space Science Systems to work with the different resolution of the two Mastcams (see Appendix A). Orthorectified Mastcam mosaics were able to be more accurately correlated to the Navcam-based map, and permitted raised ridges to be traced over the key areas of the Sheepbed member, with reference to the vertically projected M-100 mosaics when needed for higher resolution (or to correct distortions introduced in the image orthorectification process).

In addition to the large-scale mapping, a Mastcam mosaic, mcam00885, taken on sol 164, was selected for fine-detail mapping of the individual cement layers in the raised ridges and the relationship of the raised ridges to the other diagenetic features in the

Sheepbed member. This mapping was also accomplished in ArcGIS, but in this case, because it was critical that the features not be distorted, the rover-perspective white-balanced mosaic was used and the average scene pixel scale (0.206 μm/pixel) was used for measurements of the length and width of 300 individual ridges and cements.

3.4 Observations

Raised ridges within the Sheepbed mudstone occur as cracks in the mudstone filled with multiple layers of cement. The outermost layer of cement fill is resistant to erosion, resulting in curvilinear ridges that outline the original crack shape, stand above the host rock, and give these features the name "raised ridges." Interior cement layers are usually less resistant, although in some cracks multiple layers of resistant cements are visible (e.g. Figure 3.2). The redundancy in the term "raised ridges" is meant to emphasize the height of the ridges relative to their width.

Raised ridges were mapped comprehensively in the vicinity of the John Klein and Cumberland drill sites where near-rover orthorectified overhead imagery was available (Figure 3.3). Bedding is rarely visible in this local area, but it is assumed to be near-horizontal and to follow contour lines based on an observed near-horizontal conformable contact with the Gillespie Lake member [*Grotzinger et al.*, 2014]. The most obvious feature of the raised ridges at the meter scale is their clustered distribution (Figure 3.3). Laterally, a few concentrated clusters of raised ridges are visible, each region measuring tens of cm in diameter. Individual ridge networks do not continue laterally within the same contour interval (i.e. within the same stratigraphic horizon), but transition into either relatively featureless mudstone or areas of concentrated nodules and hollow nodules (e.g. Figure 3.2; [*Stack et al.*, 2014]). Additionally, both individual ridges and ridge networks cross-cut topographic contours (Figure 3.3). Some raised ridges are not localized within the larger clusters, but scattered both laterally and vertically through the mudstone. There is no consistent preferred crack orientation (Figure 3.3). At least two ridge clusters (one in Figure 3.3 and another called the "Rowatt" cluster, Figure 3.9) occur immediately beneath the Sheepbed-Gillespie Lake contact; and in one location a single raised ridge appears to cross-cut the Sheepbed-Gillespie Lake contact.

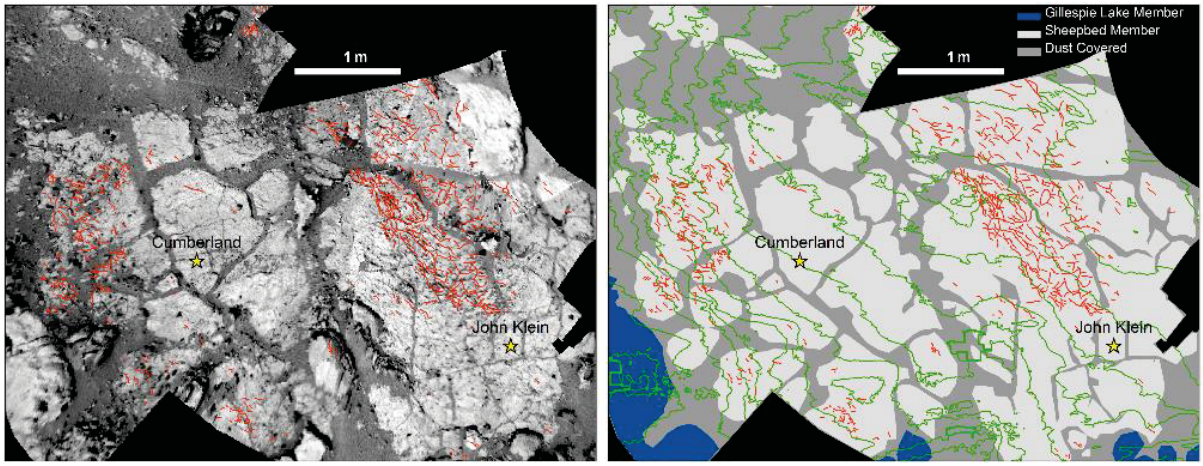

Figure 3.3 Overhead Map Showing Raised Ridge Distribution
Vertically-projected map, showing the distribution of raised ridges (red lines) throughout the mapped area. On the left side, the ridges are shown on a mosaic of rover navigation camera images. On the right side, the same mosaic is mapped to show Sheepbed member exposures in light gray, Gillespie Lake member in blue, and dust-covered regions in dark grey. Five cm contours based on the Navcam mosaic from sol 159 are shown in green. The John Klein and Cumberland drill sites are identified with yellow stars. Ridges show a clustered distribution both horizontally (within contours) and vertically (across contours) and therefore are not confined by bedding planes.

Detailed mapping of lengths, widths, and shapes of raised ridges within the dense cluster of ridges near the John Klein drill site (Figure 3.4) shows the characteristics of the crack morphologies and details of fill patterns (e.g. Figure 3.5). Erosionally resistant infill permits clear identification of the original crack morphology as represented by current ridge morphology. The raised ridges average 6.8 cm in length, but can reach up to 50 cm, and widths range between 1.1 mm to 5.6 mm, averaging 2.6 mm. Terminations of the ridges, where visible, are tapered to a spindle-shaped point. Raised ridges do not form discrete polygons; where they do intersect, it is at an arbitrary variety of angles (Figure 3.5d-f). The two-dimensional morphology of ridge exposures range from straight to sinuous (e.g. Figure 3.5). In some cases, adjacent ridges turn toward each other near the termini (e.g. Figure 3.5e).

Projection of raised ridges above the mudstone surface resulting from resistant crack-filling cement enables viewing of original crack orientation in three dimensions. Ridges range from vertical to subhorizontal in dip, and are curviplanar; several ridges are observed transitioning from sub-vertical dip angles to sub-horizontal dip angles that reflect crack intersections at oblique angles (Figures 3.5f-h). Additionally, a variety of erosionally resistant, gently sloped features, marked by parallel bands morphologically similar to ridge cement, are visible in the mudstone up to a couple of cm above the surface and are interpreted as exhumed sub-horizontal crack-fills (e.g. Figure 3.5h, i).

As noted, these raised ridges reflect initial cracks that are currently filled with two to four layers of erosionally-resistant infill. The crystal size of this cement infill is not visible, even at Mars Hand Lens Imager scales of 15-20 micrometers per pixel. The outermost cement, which represents the boundary between the sediment and the initial crack wall, is approximately 1 mm thick (measured normal to the crack surface) and has consistent thickness on all walls within individual raised ridges regardless of local curvature (i.e. it is an isopachous cement coating [*Pettijohn and Potter*, 1964]). The thickness of the cement varies in different ridge sets, from 0.6 mm to 1.2 mm (averaging 1.0 mm), but does not vary within individual ridges; within a given crack, the precipitation was isopachous. When two ridges intersect, this resistant cement continuously lines the

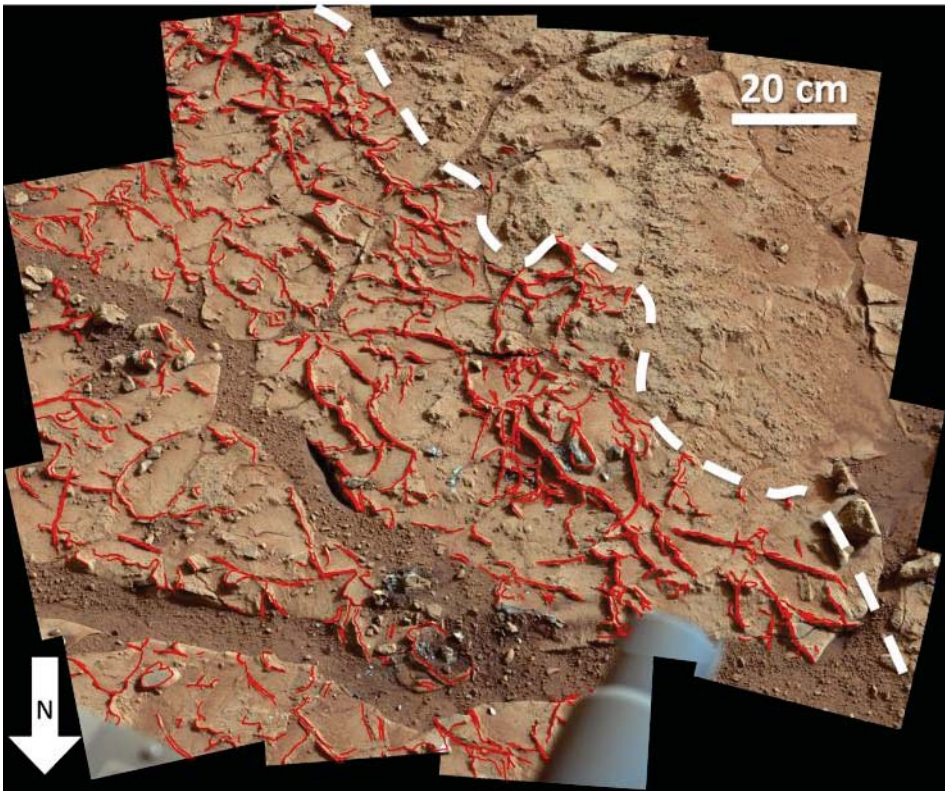

Figure 3.4 Detailed Map of Individual Raised Ridges
Detailed map of individual raised ridges (red) traced on Mastcam mosaic mcam00885 from sol 164. White dashed line highlights lateral shift in texture from raised ridges (left side) to nodules plus hollow nodules (right side).

(Figure on following page)

Figure 3.5 Panel Showing Raised Ridge Morphologies
Insets showing details of raised ridge morphology with frames from white-balanced rover-perspective mosaic mcam00885, sol 164. Scale bars for images A, D, and G are 5 cm, scale bars for insets are 1 cm. Exposed grey rock surfaces were broken by the rover wheel. Yellow arrows highlight spindle-shaped cracks with tapered termini, white arrows highlight curvilinear features for comparison to Figure 3.6. Images A-C highlight the isopachous cement lining that creates parallel-sided ridges outlining the cracks, and sometimes, as in image c, the multiple cement layers within the cracks. Image D shows that the cracks are short and taper rapidly into a spindle shape. Inset E focuses on two cracks that appear to bend towards each other, indicating that the cracks all formed in one stage and traced planes of weakness in the rock. Image F highlights the non-polygonal nature of the cracks and resulting variety of crack intersection angles. Image G shows multiple cracks that transition from near-vertical to sub-horizontal spatial orientations. Inset H highlights an intersection between a near-vertical crack and a sub-horizontal crack. Image I shows a ramped feature that appears to be a sub-horizontal raised ridge preserved because of the resistant cement.

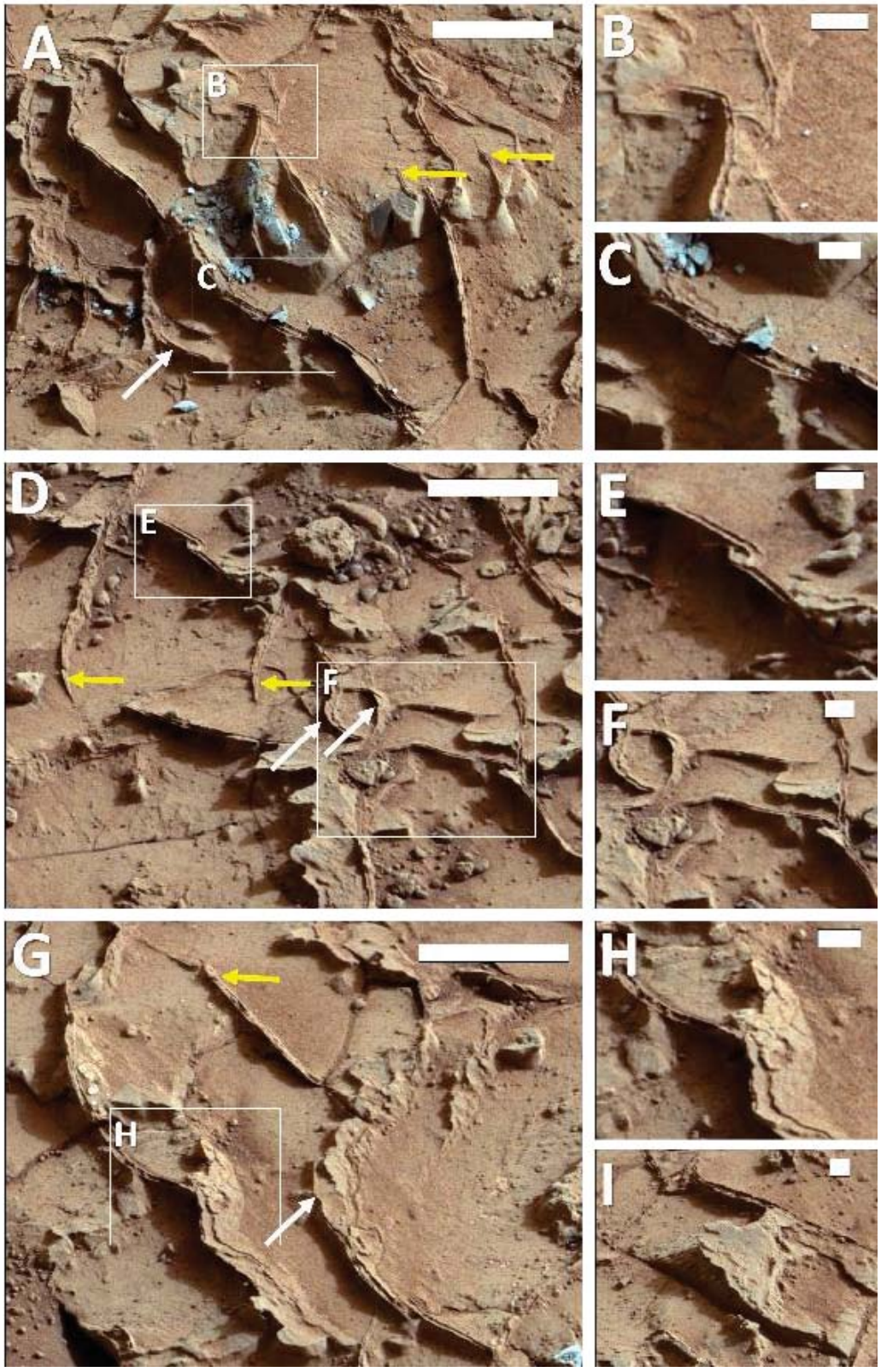
A
B
C
B
C
D
E
F
E
F
G
H
H
I

edges of the intersecting features, regardless of the orientation of the initial cracks (e.g. Figure 3.5b). No evidence is seen for detrital sediment infilling of the cracks.

The APXS, ChemCam, and CheMin instruments onboard *Curiosity* were used to explore the composition of the resistant cement fill relative to the Sheepbed mudstone [*Grotzinger et al.*, 2014; *Léveillé et al.*, 2014; *McLennan et al.*, 2014; *Vaniman et al.*, 2014]. The ChemCam instrument (laser-induced-breakdown spectroscopy) has a spot size of about 0.5 mm, and therefore was able to target laser shots along the outermost cement layer of the McGrath raised ridge target. Those analyses indicated that the outermost cement layer of the McGrath raised ridge is enriched in Mg, somewhat enriched in Li, and depleted in Al relative to the rest of the mudstone [*Léveillé et al.*, 2014]. The APXS has a 2.25 cm^2 spot area and also analyzed the sub-horizontal McGrath target, finding that the ridge was enriched in Mg and Fe, and that these were both correlated to enriched Cl relative to the Sheepbed mudstone [*McLennan et al.*, 2014]. Additionally, the CheMin x-ray diffraction instrument analyzed two samples within the Sheepbed unit, neither of which contained a visible component representing the raised ridges. The Cumberland target, however, contained a notable contribution from nodules and hollow nodules, which appears to be reflected in a several percent increase in akaganeite (an iron oxide-hydroxide/chloride mineral) and magnetite relative to the John Klein drill hole, only about 2 m away [*McLennan et al.*, 2014; *Stack et al.*, 2014; *Vaniman et al.*, 2014]. Based on these observations, it has been suggested that the resistant cement may be composed of akaganeite, magnetite, and/or some authigenic smectitic clay component, such as griffithite [*Grotzinger et al.*, 2014; *Léveillé et al.*, 2014; *McLennan et al.*, 2014; *Vaniman et al.*, 2014].

3.5 Discussion

Any proposed formation model must account for these observations: (1) Crack networks—as defined by their erosion-resistant infill—penetrate the mudstone, are spatially restricted, and transition laterally into high concentrations of nodules and hollow nodules or featureless mudstone; (2) individual cracks are curviplanar in three dimensions

and cross-cut stratigraphic contours; and (3) after opening, the cracks are filled with multiple generations of isopachous cement.

3.5.1 Origin of Raised Ridges

3.5.1.1 Formation Environment

Raised ridges within the Sheepbed mudstone appear to have originated as early diagenetic cracks within the mudstone. Their present morphology, as elevated ridges, is based on preferential erosion of the surrounding sediment relative to the crack fill (e.g. Figure 3.5b). The observation that cement continuously traces crack edges even when two cracks intersect demonstrates that the cracks were open before the cement layer began to precipitate within open void space (Figure 3.5b). Apparent spatial clustering of both nodular features [*Stack et al.*, 2014] and raised ridge networks suggests that either the distribution of one feature controlled the distribution of the other (for instance, via a change in mudstone rheology caused by the formation of one of the features), or that these are penecontemporaneous structures [e.g. *Calver and Baillie*, 1990; *Duck*, 1995]. In either case, cross-cutting relationships indicate that both nodular features and raised ridges had formed and mineralized prior to formation of late-stage, sulfate-mineralized fractures (the sulfate-mineralized fractures clearly cut through raised ridges and through nodules, shown in Figure 3.2) [*Grotzinger et al.*, 2014; *Nachon et al.*, 2014]. If raised ridges and nodules are penecontemporaneous structures, we must examine the possibility that nodules and raised ridges share a common diagenetic environment.

In addition to their distribution, a critical observation that may constrain the origin of the raised ridge features is that the cracks that comprise raised ridge networks are short, curviplanar, and have narrow to spindle-shaped terminations in three dimensions. This style of short, spindle-ended cracking occurs prior to complete lithification of the sediment [*Burst*, 1965; *Calver and Baillie*, 1990]. Additionally, cracks cross stratigraphic contours and intersect at arbitrary angles that do not form polygons (Figure 3.5). Polygonal cracking typically develops in response to internal, contractional stresses within the sediment (e.g. dewatering [*Shorlin et al.*, 2000] or cooling [*Peck and Minakami*, 1968]) wherein the polygonal morphology acts to minimize stresses within the material. Because non-

orthogonal, irregular crack intersections do not minimize stress, irregular crack orientations are typically interpreted to have formed quickly, exploiting inhomogeneities within the sediment [*Lachenbruch*, 1962; *Sletten et al.*, 2003]. Furthermore, the extension of irregular intersections in three dimensions, the curviplanar morphology of cracks which result in transitions from sub-vertical to sub-horizontal orientations, and the presence of cracks that cross-cut stratigraphic contours (i.e. cracks do not appear to either terminate or originate at common bedding planes) all indicate crack formation in the subsurface [*O'Connor*, 1972; *Horodyski*, 1976; *Plummer and Gostin*, 1981], where overburden pressures are sufficient to equalize vertical and horizontal stresses.

3.5.1.2 Comparison with Terrestrial Early Diagenetic Cracks

Combined, these lines of evidence suggest that raised ridges originated as sub-planar cracks, or voids, contained fully within the sediment. This model is very different from the most familiar mode of early diagenetic fracturing on Earth—the formation of desiccation cracks. Desiccation cracks form at the sediment-air interface because water loss leads to contraction of the sediment [*Lachenbruch*, 1962; *Plummer and Gostin*, 1981]. Such desiccation features originate at a discrete sedimentary surface (a future bedding plane), and extend vertically into the subsurface, forming a wedge shape that narrows and ultimately terminates at some depth (often at variable depths) within the sediment [*Weinberger*, 1999]. Although early stages of crack formation may be recognized by the presence of short, isolated cracks (e.g. “incomplete mudcracks”, [*Plummer and Gostin*, 1981]), these initial cracks typically expand and intersect in a polygonal pattern to minimize contractional stresses within the surface layers [*Sletten et al.*, 2003]. Regardless of the extent to which this ultimate, polygonal morphology is reached, desiccation cracks that enter the rock record are invariably filled by detrital sediment from the sediments that directly overlie the desiccated strata [*Pettijohn and Potter*, 1964]. Indeed, desiccation cracks in the rock record are recognized by the sediments that fill them. This is in sharp contrast to the Sheepbed cracks, which were neither filled with fine-grained Sheepbed sediment nor relatively coarse-grained sands from the Gillespie Lake sediment, but instead

show multiple isopachous cement layers. Furthermore, the Sheepbed cracks are curviplanar in three dimensions and do not form polygons or terminate along bedding planes.

Although less common, subaqueous cracking of sediments is not unknown in terrestrial environments (e.g. Figure 3.6). Subaqueous crack formation was first recognized by White [1961], who suggested that subaqueous cracks could result from *in situ* salinity changes in clay colloids leading to fabric collapse and then contraction and tighter packing of the clays. This process generates crack-shaped voids that are filled with the displaced fluids (Figure 3.7a). The term "synaeresis" was applied to these cracks to refer to the contractional stresses within the sediment that resulted during fabric collapse within the clay [*White*, 1961]. The potential for saline fluids to result in such volumetric shrinkage was experimentally confirmed by Burst [*Burst*, 1965], and the resulting features share many commonalities with raised ridges in the Sheepbed mudstone. For instance, synaeresis cracks tend to be short, straight to sinuous, are generally spindle-shaped, with tapering termini [*O'Connor*, 1972; *Plummer and Gostin*, 1981], form in the very shallow subsurface (all predate sediment compaction), and cross-cut bedding planes [*Horodyski*, 1976; *Plummer and Gostin*, 1981]. Additionally, the presence of a significant amount of smectite clays within the Sheepbed mudstone [*McLennan et al.*, 2014; *Vaniman et al.*, 2014] suggest that environmental conditions may have been favorable for saline-fluid-based synaeresis (Figure 3.7a).

More recently, several additional formation processes for synaeresis cracks have been proposed. In one alternative, synaeresis-like features result from tensional stresses imposed upon sediment from an external source [*Cowan and James*, 1992; *Pratt*, 1998b; a; *Bishop et al.*, 2006]. One subcategory of cracks that clearly form by this mechanism, termed "diastasis" cracks [*Cowan and James*, 1992], are sub-planar, sub-vertical, often well-aligned spindle-shaped cracks that form in clay-rich, cohesive layers as these layers are placed under tension from wave-driven motion of overlying and underlying sandy, or less cohesive, layers. Rupture of the cohesive layer permits rapid infilling of diastasis cracks via injection of less cohesive sediment from either above or below the cohesive layer. A critical observation leading to the interpretation of diastasis cracks, however, is

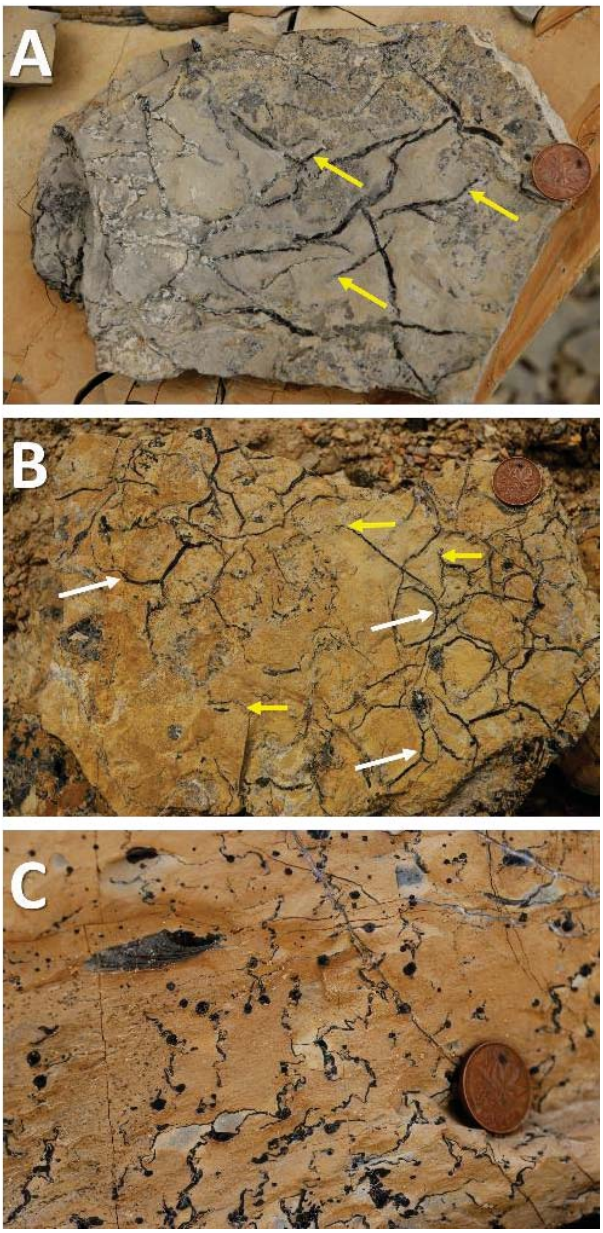

Figure 3.6 Proterozoic Molar Tooth Structure Analogs
Proterozoic molar tooth structures from the Helena formation in the Belt Supergroup, MT, USA. Coin is 19 mm across for scale. Images a and b show preserved bedding planes with short, curvilinear, spindle-shaped cracks. Yellow arrows highlight spindle-shaped cracks with tapered termini, white arrows highlight curvilinear features for comparison to Figure 3.5. These crack morphologies are very comparable to the raised ridge crack morphologies, although the cement is not resistant to erosion in this case. Note curvilinear cracks and irregular clustered distribution in image b. Image c shows a cross-section of molar tooth ribbons and blobs. Note interfingering transition between ribbon and blob facies and horizontal-to-vertical transitions of ribbons.

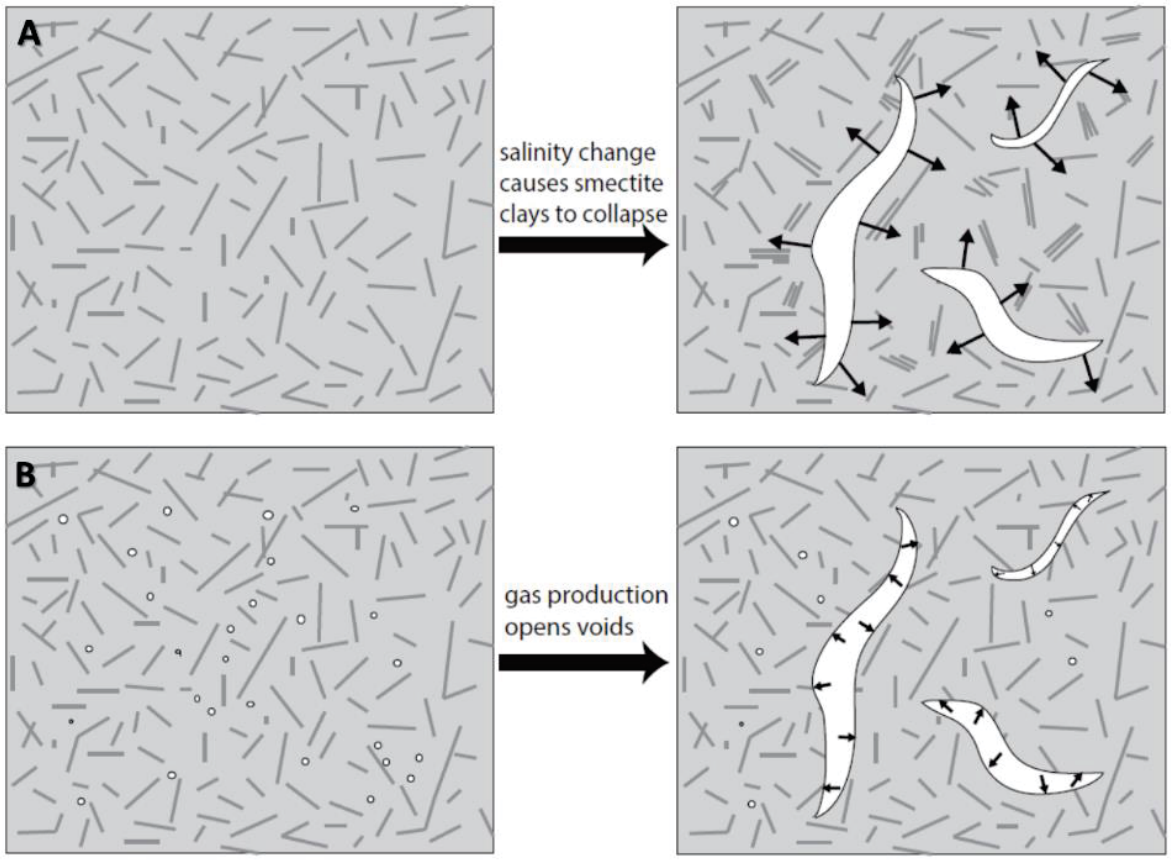

Figure 3.7 Schematic of Synaeresis Crack Formation Mechanisms
Schematic showing possible formation mechanisms for synaeresis crack formation. (A) depicts a change in pore fluid chemistry that causes collapse of smectite clay interlayers, causing volumetric compaction of the sediment, which opens synaeresis cracks. (B) depicts a gas production process such that if the gas becomes trapped, it can create void spaces within the mudstone, which could form both hollow nodules and synaeresis or raised ridge shapes.

the presence of systematic crack orientations resulting from a directed tensional stress field. Raised ridges within the Sheepbed mudstone show no such preferred orientation (see Figure 3.3), suggesting that diastasis is an unlikely mechanism of formation. A similar formation mechanism that does not require layered sediments suggests that these cracks could open due to shaking of the sediment from nearby seismic activity (possibly due to landslides or impacts in this case) even in homogeneous cohesive material [*Pratt*, 1998b; a]. This mechanism would not produce aligned cracks and so cannot be ruled out for the raised ridge features.

In a third scenario, synaeresis-like cracks are inferred to result from the production of gasses within sedimentary pore-fluids, creating localized dilational stresses within the sediment. On Earth, Proterozoic "molar-tooth" structures are typically interpreted to have formed this way [*Smith*, 1968; *Plummer and Gostin*, 1981; *Furniss et al.*, 1998]. Predictable behavior resulting from the production (or exsolution) of gas within pore fluids of the surrounding sediment [*Terzaghi*, 1944; *Mitchener and Torfs*, 1996; *Pollock et al.*, 2006; *Stack et al.*, 2014] creates structures that provide an interesting comparison to the morphology of primary void spaces within the Sheepbed mudstone. The primary parameter in determining the behavior of gasses within unconsolidated substrate is the cohesive strength of the sediment [*Terzaghi*, 1944], which commonly reflects a combination of grain size and composition. Composition is critical because the presence of >15% clay minerals within the sediment has been shown to substantially increase its cohesive strength [*Mitchener and Torfs*, 1996]. Once gasses form bubbles that are larger than inter-particle void space, these bubbles will provide dilational stresses that deform and compact the surrounding sediment. Because gasses will tend to rise and escape, grain-scale inhomogeneities will be exploited and favor the upward movement of gas. In the case of poorly consolidated sediments, upward migration of gas bubbles will often result in dewatering and an increase in the consolidation of sediments. In the case of higher strength sediments (such as cohesive, and clay-rich sediments), gas bubbles will tend to be trapped as consolidation of grains along the bubble margin increases local sediment strength. Under these conditions, crack formation can occur when gas pressures exceed the local sediment yield strength, and cracks will commonly propagate in a range of orientations, from vertical

(denoting the favored orientation for gas escape) to horizontal (denoting a common direction of weakness within layered sediment) [*Pollock et al.*, 2006].

Exsolution of gasses within substrate pore space has recently been proposed as a mechanism for the formation of nodules and hollow nodules within the Sheepbed mudstone [*Stack et al.*, 2014]. A mechanism of void formation resulting from release of sediment gasses can plausibly explain both the formation of early diagenetic hollow nodules [*Stack et al.*, 2014] and cracks associated with the raised ridges. Differences in the morphology of gas-induced structures may reflect either differences in the rate of production of gasses within the sediment or spatial differences in the cohesive strength of the sediment [*Pollock et al.*, 2006]. *Stack et al.* [2014] further suggest a combination of these last two mechanisms of crack formation, in which release of pore-fluid gasses may plausibly be related to the propagation of impact-induced seismic waves during deposition of the Yellowknife Bay formation. In this scenario, complex interference patterns could produce zones of greater or lesser seismic pressure, which might affect the extent to which pressure-induced degassing occurs, and thereby control the spatial distribution of nodular features and crack networks. Similarly, slight changes in the cohesive strength of the substrate, resulting from either differential compaction or spatial differences in clay content, may be reflected in the spatial distribution of gas-induced features.

Formation of raised ridges as curviplanar voids in the subsurface formed via gas expansion supports the observations of crack clustering and the cross-cutting of stratigraphic contour intervals. Similarly, such a mechanism supports the varied orientation of observed features, which presumably reflect lithologic zones of weakness and inhomogeneities in the sediment (Figure 3.3). Finally, the observation of multiple clusters of raised ridges directly beneath and, in one case, intersecting the Gillespie Lake member suggest that crack formation must have occurred penecontemporaneously with or soon after deposition of the basal Gillespie Lake sandstone. These observations suggest that crack formation occurred prior to burial-induced dewatering, and provide the possibility that the relatively coarse-grained Gillespie Lake member may have provided critical overburden pressure necessary to increase gas pressures during exsolution of gasses within Sheepbed pore-fluids.

3.5.2 Lithification of Raised Ridges

Regardless of the formation mechanism of sub-planar cracks and voids within the Sheepbed mudstone, it is necessary to discuss their mechanism of preservation. Fine-grained sediment can preserve cracks formed during or shortly after sediment deposition under several distinct conditions. First, there is a possibility that sediment is sufficiently lithified via early cementation so that it can retain otherwise unsupported void space. However, more commonly, the void space fills with sediment or detritus or is propped open by cement that occludes porosity [*Halley and Schmoker*, 1983]. In general, if cracking occurs at the sediment-water (or sediment-air) interface, cracks will typically be filled with sediment from above [*Pettijohn and Potter*, 1964]. Similarly, subaqueous shrinkage cracks formed via diastasis will typically be filled with sediment injected from less cohesive sedimentary units either directly above or below the cracked horizon [*Cowen and James,* 1992]. By contrast, subaqueous cracks on Earth that originate from gas expansion are commonly filled with *in situ* mineral precipitates [*Furniss et al.,* 1998; *Bishop and Sumner,* 2006; *Pollock et al.,* 2006]. In the case of the Sheepbed features, after crack formation, voids were filled by a succession of isopachous cement layers. The initial erosion-resistant cement layer is approximately 1 mm thick, measured normal to the crack surface, regardless of local curvature, and thus provides an equal-thickness coating on all available surfaces. Isopachous coatings indicate that the cement was precipitated in a phreatic, or water-saturated, environment (e.g. [*Longman*, 1980; *Amieux et al.*, 1989]). Erosionally-resistant isopachous cement is the defining attribute of the raised ridges throughout the observed Sheepbed member and likely reflects pore-fluid chemistry, or the chemical interaction between pore-fluids and released gasses, at the time of crack formation.

After this initial cement was deposited, an erosionally less-resistant cement precipitated within the remaining void space, further infilling and occluding the porosity. In wider cracks, this was followed by another erosionally resistant cement layer, and, if residual porosity remained it was occluded by a final, erosionally less-resistant cement. This type of layered and laterally repeated cementation of voids is common on Earth where it is utilized in "cement stratigraphy" [*Evamy*, 1969; *Meyers*, 1991], a methodology where

sequences of different cement layers are traced on a regional scale and used to map ancient groundwater or pore water systems [*Grover and Read*, 1983; *Kaufman et al.*, 1988]. Different cement layers are usually attributed to evolving fluid chemistries, and sometimes related to distinct fluid flow events [*Meyers*, 1974; *Meyers and Lohmann*, 1985; *Dorobek*, 1987]. In the raised ridges, variation in erosional resistance of successive cement layers most likely indicates a change in cement composition that reflects changes in the pore fluid chemistry. Such interpretation is supported by the ChemCam observation that the outermost resistant cement is enriched in Mg and depleted in Al relative to the interior layers [*Léveillé et al.*, 2014]. At present, it is impossible to constrain the detailed timing of these different cement layers. Once the initial erosionally resistant cement was precipitated, it would have acted to reinforce void walls, permitting voids to potentially remain open for extended periods of time. The absence, however, of significant calcium sulfate mineralization within the cracks suggests that cementation of the raised ridges was complete prior to late-stage hydrofracture of the Yellowknife Bay formation [*Grotzinger et al.*, 2014; *Nachon et al.*, 2014].

3.5.3 Formation Summary and Comparison with Earth Analogs

Key first-order interpretations that we can derive from observations of the raised ridges are (1) the cracks formed during early diagenesis of the Sheepbed mudstone, (2) the cracks formed in a near-isotropic stress environment created by overburden pressure from overlying sediments, (3) mineral precipitation within the crack initiated soon after crack formation in a water-saturated environment, and proceeded with a series of precipitated cements of differing mineralogy and/or resistance to erosion, and (4) the morphology and distribution of the Sheepbed cracks matches the characteristics identified for synaeresis cracks, which form via sediment contraction with pore-fluid salinity changes, mechanical shaking, exsolution of pore-fluid gasses, or some combination thereof.

Having established this set of constraints concerning the early diagenetic, subsurface, pore-fluid saturated environment in which the raised ridges formed and filled, the remaining challenge is to evaluate the set of synaeresis crack formation hypotheses for applicability to the Sheepbed member structures based on Earth analogs. Although

isolating specific crack formation mechanisms for subaqueous/shallow burial conditions is difficult for ancient sedimentary rocks, even on Earth, because of the absence of good modern analogs [e.g. *Smith*, 1968; *Frank and Lyons*, 1998; *Furniss et al.*, 1998; *James et al.*, 1998; *Pratt*, 1998a; *Marshall and Anglin*, 2004], the observations of the Sheepbed member and the restricted set of plausible environments on Mars help constrain the likely possibilities.

The most accepted hypotheses for synaeresis crack formation, as discussed, include (1) pore-fluid salinity changes causing clay layer collapse and volumetric shrinkage of the sediment, (2) mechanical shaking of the sediments causing tensional stresses, and (3) gas production in the sediment creating dilational stresses. Key observations in the Sheepbed unit that must be explained by the specific formation hypothesis include the clustered, irregular distribution of raised ridges, the lack of a preferred ridge orientation, and the cement (rather than sediment) crack infill.

Pore-fluid salinity changes causing clay layer collapse create synaeresis cracks preferentially in clay-rich areas [*White*, 1961; *Burst*, 1965]. This method of crack formation could create a clustered distribution of raised ridges if clay-rich zones were heterogeneously distributed in the mudstone. Although this is not specifically constrained by *Curiosity's* observations, since only two holes were drilled and sampled for XRD mineral compositions, it is plausible given the presence of smectite within the unit and the compositional differences between the John Klein and Cumberland drill sites [*McLennan et al.*, 2014; *Vaniman et al.*, 2014]. Preferred ridge orientations would not be expected for this formation mechanism as cracks would follow inhomogeneities in the sediment. Although cracks formed in this manner on Earth are usually preserved by sediment infill rather than precipitated cements, this mechanism for forming void spaces cannot be ruled out for the Sheepbed raised ridges.

Earthquake-induced shaking [*Cowan and James*, 1992; *Fairchild et al.*, 1997; *Pratt*, 1998b; a] or repeated wave action [*James et al.*, 1998; *Bishop et al.*, 2006] mechanically breaking up cohesive but unlithified sediments have also been used to explain synaeresis crack formation. There is no evidence for wave-induced sedimentary structures in the Sheepbed mudstone [*Grotzinger et al.*, 2014] and seismicity is rare on Mars

[*Anderson et al.*, 1977; *Golombek et al.*, 1992], however, impact-induced shaking could be a possible Martian alternative for mechanical shaking of sediments to form synaeresis cracks. The clustered distribution of cracks in the Sheepbed could be based on slight lithological differences in the sediment. However, cracks formed by this mechanism are inevitably preserved in ancient rocks by sediment infill rather than mineral precipitation, so this is not a favored hypothesis for the Sheepbed raised ridges.

Whereas both salinity changes and mechanical shaking could viably have occurred during deposition of the Sheepbed mudstone, the most distinctive characteristic of the raised ridges relative to the majority of terrestrial synaeresis cracks is that they are filled with cement, rather than sediment (e.g. [*White*, 1961; *Pettijohn and Potter*, 1964; *Burst*, 1965; *Cowan and James*, 1992]). The one notable terrestrial example of a class of synaeresis cracks where cement rather than sediment fills the voids is called "molar tooth" and the production of these structures is most often attributed to gas production in the subsurface [*Bauerman*, 1885; *Furniss et al.*, 1998; *Pollock et al.*, 2006]. This gas formation hypothesis predicts an irregular distribution of synaeresis cracks and other diagenetic morphologies based on minor differences in sediment lithology, and does not predict a preferred ridge orientation. Furthermore, molar tooth cracks are always filled with cement; the cements that fill molar tooth cracks precipitate so early that sometimes they are reworked during current scouring, leaving void-fill present as sedimentary clasts in immediately overlying beds [*Smith*, 1968; *O'Connor*, 1972; *James et al.*, 1998; *Bishop et al.*, 2006]. In terrestrial environments, these void-filling cements are primarily calcite, although in at least one location, early diagenetic saponite (presently talc) likely precipitates as cement [*Tosca et al.*, 2011]. Raised ridges within the Sheepbed member similarly contain early diagenetic cement infill, potentially smectite, and/or a chlorite phase such as akaganeite [*Léveillé et al.*, 2014; *McLennan et al.*, 2014].

The multiple morphologies of terrestrial "molar tooth" textures, all interpreted as due to gas production in the subsurface, invite further comparison with the diagenetic textures in the Sheepbed unit. The most common molar tooth morphologies are "ribbons" and "blobs" [*O'Connor*, 1972]. In scale and morphology, "ribbons", the synaeresis-like components of molar tooth structure, are very similar to the raised ridges in the Sheepbed

unit; they are narrow, at times sinuous, spindle-terminated cement-filled fractures and they are observed to transition between horizontal and vertical dimensions (Figure 3.6) [*O'Connor*, 1972; *Horodyski*, 1976; *Plummer and Gostin*, 1981]. Molar tooth "blobs" are typically mm- to cm-scale spheroidal pockets, suggested to have formed as gas bubbles, either interfingered with the ribbons or in separate clusters, filled with the same calcite cement [*O'Connor*, 1972; *Pollock et al.*, 2006]. These blobs may be comparable to the early diagenetic hollow nodules described in the Sheepbed unit as rimmed, erosion-resistant, spheroidal structures about 1.2 mm in diameter, that are clustered in some locations and laterally transition into raised ridge clusters [*Grotzinger et al.*, 2014; *Stack et al.*, 2014]. Both the ribbon and blob morphologies are explained by gas production in mudstone, where slight variations in lithology and cementation or in localized gas production have been used to explain transitions between unaltered mudstone, blobs, and ribbons [*Pollock et al.*, 2006]. These features are illustrated in Figure 3.6 with arrows pointing out the features that are also visible in the Sheepbed raised ridges (Figure 3.5). It is important to note that the cements that fill molar tooth structures are not isopachous and are not resistant relative to the surrounding rock, so the three-dimensional structure (including the sub-vertical to sub-horizontal transitions) is only visible when looking at the rock in cross-section (e.g. Figure 3.6c). However, comparison of the two-dimensional crack shapes reveals the similarity in spindle terminations, curvilinear crack geometry, clustered distribution, and transitions between morphologies. In summary, although the composition and style of the infilling cement in the Sheepbed unit is distinct from that usually found in molar tooth structures, the analog is unique because it is filled by cement rather than sediment, and because it suggests that gas formation or a similar single formation mechanism could potentially create more than one of the early diagenetic morphologies in the Sheepbed unit. This would fit with the observations of lateral transitions between diagenetic textures.

3.6 Summary

- Resistant cement-filled cracks ("raised ridges") in the Sheepbed mudstone were observed and mapped using imagery from the *Curiosity* rover.

- The raised ridges are shown to be early diagenetic features based on lateral transitions with other diagenetic textures. Later sulfate-filled veins crosscut these early diagenetic features.
- Comparison with analogous early diagenetic mud crack morphologies indicates that the raised ridges are synaeresis cracks (subaqueous shrinkage cracks).
- Isopachous cement fills with differing erosion-resistance likely represent a series of different cements indicating changing pore-fluid chemistries within the phreatic zone.
- Synaeresis crack formation mechanisms viable in the Sheepbed unit include pore fluid salinity changes causing volumetric shrinkage of smectitic clay fabrics, impact-induced mechanical shaking, or gas production.
- Proterozoic molar tooth structures, formed by gas production, provide an intriguing analog for the raised ridges because they (1) are cement-filled and (2) have multiple morphologies comparable to the diagenetic morphologies in the Sheepbed mudstone.

3.7 Appendix

3.7.1 Description of Processing of Mastcam Images

Mastcam images are acquired at 12 bits, with the noise level captured by the least significant bit. The data are then converted to 8-bit using an 11-bit lookup table. Although several tables exist, a modified square-root table (Figure 3.8) was used to encode the vast majority of the images. This table will encode multiple input values to a single output value, approximating the statistical variation of the signal. After encoding, the images are stowed within the camera's large buffer memory. When downlinked, the images can be compressed with a predictive lossless compressor, or more normally, with a JPEG compressor with selectable quality factor. Typically quality factors of 85 or higher are used for geology targets.

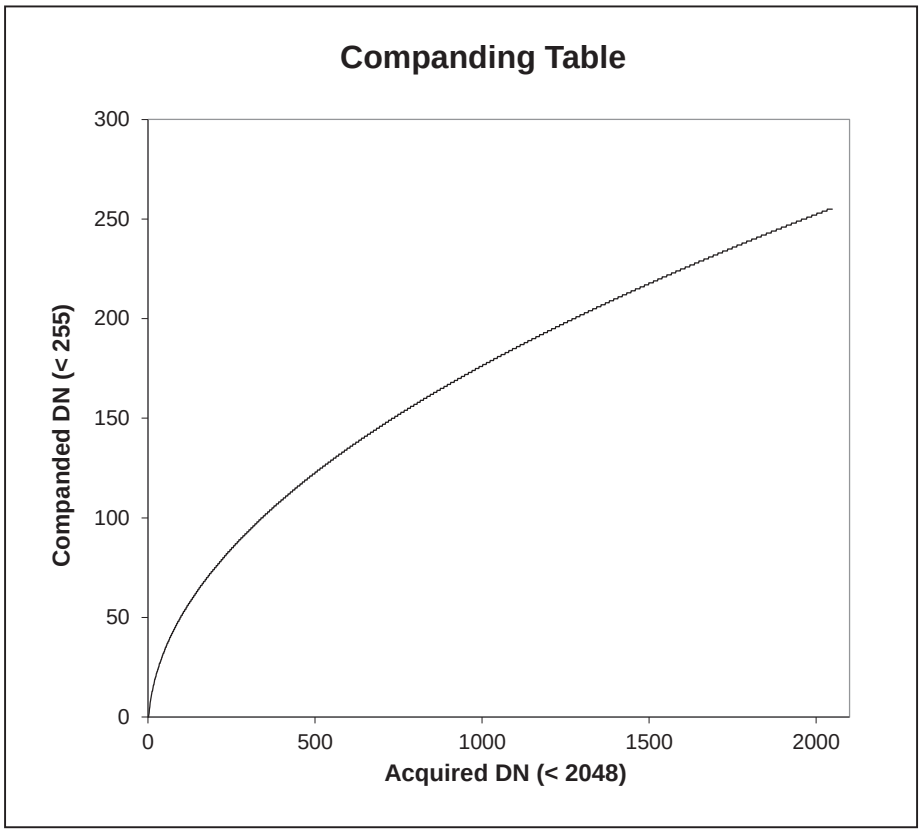

Figure 3.8 Plot of Mastcam Image Companding Table
Modified square-root companding table used to encode the images in *Curiosity*'s Mastcam buffer. Encodes multiple input values into a single output value to approximate the signal's statistical variability.

3.7.1.1 Radiometric ground image processing

Radiometric ground image processing proceeds as follows: images are first decompressed and then expanded back to their original dynamic range using an inverse of the encoding table; no interpolation is applied in an attempt to recover the full variance around each mean value. For computational convenience, these data are stored in 16-bit words. A temperature dependent correction is then applied to adjust for thermally-generated electrons (noise). For short exposures, an electronic shutter smear correction is applied (generally, the images used in this study did not need this correction). A flat field correction is then applied to cancel lens brightness non-uniformity. The final photometric process is to adjust for detector sensitivity to create radiance images. Images that have gone through this processing are available through the Planetary Data System (PDS) as Reduced Data Records (RDR), designated by the letters in the Picture ID *_DRXX.IMG.

3.7.1.2 Geometric image processing

Geometric processing proceeds as follows: each image is geometrically linearized to remove camera lens distortion and prepare the image for further geometric processing. Images at this stage of processing are also available from the PDS as *_DRLX.IMG products. This processing is further described in the Mastcam/MAHLI/MARDI Software Interface Specification [*NASA-JPL*, 2013].

Images acquired as stereoscopic sets (pairs or larger mosaics) are aggregated into a separate directory and processed by a modification of the Ames Stereo Pipeline created by Mastcam Co-Investigator Laurence Edwards. This processing includes five steps. First relevant acquisition parameters are extracted from each image's metadata, its analogous pair is identified, and the images are converted from the PDS format to an internal format. Second, an image alignment is performed along with a reprojection transformation using the camera models (required because the two Mastcameras have disparate focal lengths). By default, the alignment and reprojection produces an epipolar aligned image pair, although other schemes can be chosen for unusual imaging geometries. Third, stereoprocessing of each image pair is completed: a filter is applied to each image that enhances edges and reduces sensitivity to differing lighting conditions. A pyramidal

correlation scheme utilizing 3 or more reduced scale versions of each image and a fixed-sized correlation window quickly generate disparity search constraints. The initial search constraints are used as input to an integer correlator stage operating on the full resolution images. The results from the integer correlator are in turn utilized by a sub-pixel correlator stage generating dense high-resolution disparity maps with sub-pixel accuracy, and then automated pruning of bad correlations, based on a bi-directional consistency check and numerical confidence levels computed by the correlation software, occurs at each stage. Fourth, the final sub-pixel disparity map is interpolated and smoothed, and the camera models are used to generate 3D coordinates for each pixel where a valid match was determined. Fifth, output from each run includes intermediate processing images used in correlation, a pointcloud, XYZ maps, and mesh models in SGI OpenInventor format, with textures derived from the higher resolution camera image data (right eye). For multiple image stereo mosaics, an index mesh collection file is also created. All 3D data is in rover navigation coordinates.

The output of the stereo processing can be viewed in Triangulated Integrated Network (TIN) format in software capable of reading SGI *.iv files. For further processing into Digital Terrain Models (DTMs) and associated orthographic map projected images, the TIN to DTM conversion capability of the Ames Research Center Antares visualization software is employed. This software resamples the mesh into height and texture raster images, allowing the user to specify the sampling interval, interpolating where necessary. The final output consists of two GeoTiff image files: a signed 32-bit DEM, and a 24-bit (8 bits per channel) color texture image, both in orthographic projection, with labels in GeoTiff format and local site coordinates.

3.7.2 Location of Raised Ridges targeted by ChemCam

Raised ridge clusters outside of the range of Figure 3.3 that were targeted by ChemCam include Rowatt and Discovery Creek. The locations of these images in the Sheepbed unit are shown in Figure 3.9 along with the rover traverse through Yellowknife Bay.

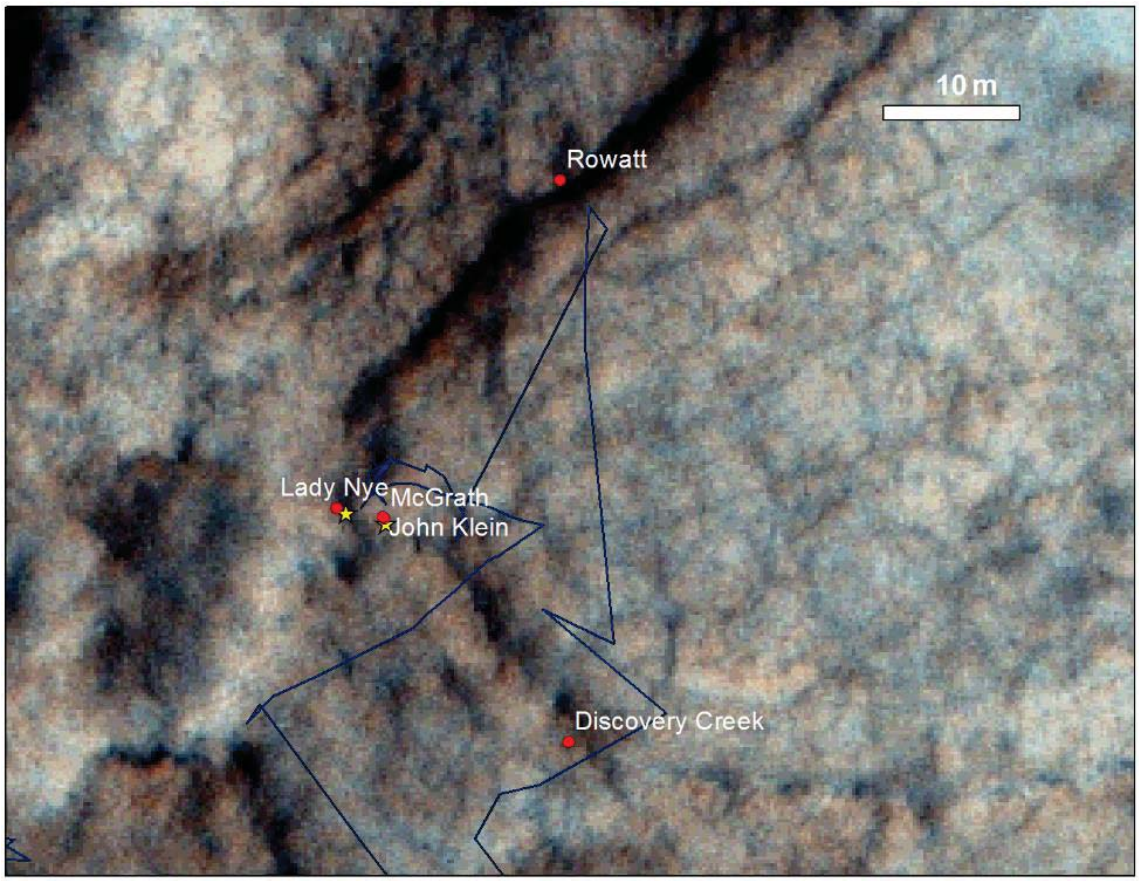

Figure 3.9 Map Showing Raised Ridge ChemCam Targets
Map showing locations of all raised ridge targets (red circles) that were shot by the ChemCam LIBS instrument. Yellow stars show drill sites, Cumberland on the left and John Klein on the right. Dark blue path represents rover traverse.

Acknowledgments

This work was supported by NASA Mars Science Laboratory grant 1449659 to JPG. We are grateful to our Mars Science Laboratory science team colleagues for helpful discussions, and particularly thank science team members J. Schieber and D. Oehler for helpful comments on an earlier version of this manuscript. Comments from two anonymous reviewers further improved this manuscript.

REFERENCES

Alvarez, L. W., W. Alvarez, F. Asaro, and H. V. Michel (1980), Extraterrestrial Cause for the Cretaceous-Tertiary Extinction, *Science*, *208*(4448), 1095-1108, doi: 10.1126/science.208.4448.1095.

Amieux, P., P. Bernier, R. Dalongeville, and V. Demedwecki (1989), Cathodoluminescence of Carbonate-Cemented Holocene Beachrock from the Togo Coastline (West-Africa) - an Approach to Early Diagenesis, *Sedimentary Geology*, *65*(3-4), 261-272, doi: 10.1016/0037-0738(89)90028-6.

Anderson, D. L., W. F. Miller, G. V. Latham, Y. Nakamura, M. N. Toksoz, A. M. Dainty, F. K. Duennebier, A. R. Lazarewicz, R. L. Kovach, and T. C. D. Knight (1977), Seismology on Mars, *Eos T Am Geophys Un*, *58*(8), 828-828.

Anderson, R. B., and J. F. Bell (2010), Geologic mapping and characterization of Gale Crater and implications for its potential as a Mars Science Laboratory landing site, *The Mars Journal*, *5*, 76-128, doi: 10.1555/mars.2010.0004.

Arvidson, R. E., et al. (2014), Ancient Aqueous Environments at Endeavour Crater, Mars, *Science*, *343*(6169), doi: 10.1126/science.1248097.

Bakalowicz, M. J., D. C. Ford, T. E. Miller, A. N. Palmer, and M. V. Palmer (1987), Thermal Genesis of Dissolution Caves in the Black Hills, South-Dakota, *Geological Society of America Bulletin*, *99*(6), 729-738, doi: 10.1130/0016-7606(1987)99<729:Tgodci>2.0.Co;2.

Baker, M. B., and J. R. Beckett (1999), The origin of abyssal peridotites: a reinterpretation of constraints based on primary bulk compositions, *Earth Planet Sc Lett*, *171*(1), 49-61, doi: 10.1016/S0012-821x(99)00130-2.

Baker, V. R., and D. J. Milton (1974), Erosion by Catastrophic Floods on Mars and Earth, *Icarus*, *23*(1), 27-41, doi: 10.1016/0019-1035(74)90101-8.

Banner, J. L., and G. N. Hanson (1990), Calculation of Simultaneous Isotopic and Trace-Element Variations during Water-Rock Interaction with Applications to Carbonate Diagenesis, *Geochim Cosmochim Ac*, *54*(11), 3123-3137, doi: 10.1016/0016-7037(90)90128-8.

Bauerman, H. (1885), Report on the geology of the country near the forty-ninth parallel of North latitude West of the Rocky Mountains. Report of Progress 1882-1884, Part B, Geological Survey of Canada (1885), pp. 1-42.

Belderson, R. H., N. H. Kenyon, and A. H. Stride (1978), Local Submarine Salt-Karst Formation on Hellenic Outer Ridge, Eastern Mediterranean, *Geology; Geology*, *6*(12), 716-720, doi: 10.1130/0091-7613(1978)6<716:Lssfot>2.0.Co;2.

Bell, J., A. Godber, M. Rice, A. Fraeman, B. Ehlmann, W. Goetz, C. Hardgrove, D. Harker, J. Johnson, and K. Kinch (2013), Initial Multispectral Imaging Results from the Mars Science Laboratory Mastcam Investigation at the Gale Crater Field Site, paper presented at 44th Lunar and Planetary Science Conference, LPI, Houston, TX, Abs. #1417.

Bethke, C. M. (1985), A Numerical-Model of Compaction-Driven Groundwater-Flow and Heat-Transfer and Its Application to the Paleohydrology of Intracratonic Sedimentary Basins, *J Geophys Res-Solid*, *90*(Nb8), 6817-6828, doi: 10.1029/JB090iB08p06817.

Bibring, J. P., et al. (2005), Mars surface diversity as revealed by the OMEGA/Mars Express observations, *Science*, *307*(5715), 1576-1581, doi: 10.1126/science.1108806.

Bibring, J. P., et al. (2006), Global mineralogical and aqueous mars history derived from OMEGA/Mars Express data, *Science*, *312*(5772), 400-404, doi: 10.1126/science.1122659.

Bish, D., et al. (2014), The first X-ray diffraction measurements on Mars, *IUCrJ*, *1*(Pt 6), 514-522, doi: 10.1107/S2052252514021150.

Bish, D. L., et al. (2013), X-ray Diffraction Results from Mars Science Laboratory: Mineralogy of Rocknest at Gale Crater, *Science*, *341*(6153), doi: 10.1126/science.1238932.

Bishop, J. W., D. Y. Sumner, and N. J. Huerta (2006), Molar tooth structures of the Neoarchean Monteville Formation, Transvaal Supergroup, South Africa. II: A wave-induced fluid flow model, *Sedimentology*, *53*(5), 1069-1082, doi: 10.1111/j.1365-3091.2006.00802.x.

Blake, D., et al. (2012), Characterization and Calibration of the CheMin Mineralogical Instrument on Mars Science Laboratory, *Space Sci Rev*, *170*(1-4), 341-399, doi: 10.1007/s11214-012-9905-1.

Blaney, D. L., et al. (2014), Chemistry and texture of the rocks at Rocknest, Gale Crater: Evidence for sedimentary origin and diagenetic alteration, *J Geophys Res-Planet*, *119*(9), 2109-2131, doi: 10.1002/2013je004590.

Bryan, W. B., L. W. Finger, and F. Chayes (1969), Estimating proportions in petrographic mixing equations by least-squares approximation, *Science*, *163*(3870), 926-927, doi: 10.1126/science.163.3870.926.

Burr, D. M., P. A. Carling, and V. R. Baker (Eds.) (2009), *Megaflooding on Earth and Mars*, 319 pp., Cambridge University Press, New York.

Burst, J. F. (1965), Subaqueously Formed Shrinkage Cracks in Clay, *Journal of Sedimentary Petrology*, *35*(2), 348-353.

Calver, C. R., and P. W. Baillie (1990), Early Diagenetic Concretions Associated with Intrastratal Shrinkage Cracks in an Upper Proterozoic Dolomite, Tasmania, Australia, *Journal of Sedimentary Petrology*, *60*(2), 293-305.

Campbell, J. L., G. M. Perrett, R. Gellert, S. M. Andrushenko, N. I. Boyd, J. A. Maxwell, P. L. King, and C. D. M. Schofield (2012), Calibration of the Mars Science Laboratory Alpha Particle X-ray Spectrometer, *Space Sci Rev*, *170*(1-4), 319-340, doi: 10.1007/s11214-012-9873-5.

Canfield, D. E. (2005), THE EARLY HISTORY OF ATMOSPHERIC OXYGEN: Homage to Robert M. Garrels, *Annual Review of Earth and Planetary Sciences*, *33*(1), 1-36, doi: 10.1146/annurev.earth.33.092203.122711.

Carr, M. H. (1987), Water on Mars, *Nature*, *326*(6108), 30-35, doi: 10.1038/326030a0.

Carrapa, B., A. Di Giulio, and J. Wijbrans (2004), The early stages of the Alpine collision: an image derived from the upper Eocene–lower Oligocene record in the Alps–Apennines junction area, *Sedimentary Geology*, *171*(1-4), 181-203, doi: 10.1016/j.sedgeo.2004.05.015.

Cawood, P. A., A. A. Nemchin, M. Freeman, and K. Sircombe (2003), Linking source and sedimentary basin: Detrital zircon record of sediment flux along a modern river system and implications for provenance studies, *Earth Planet Sc Lett*, *210*(1-2), 259-268, doi: 10.1016/S0012-821x(03)00122-5.

Chesworth, W., J. Dejou, and P. Larroque (1981), The Weathering of Basalt and Relative Mobilities of the Major Elements at Belbex, France, *Geochim Cosmochim Ac*, *45*(7), 1235-1243, doi: 10.1016/0016-7037(81)90147-2.

Christensen, P. R., et al. (2005), Evidence for magmatic evolution and diversity on Mars from infrared observations, *Nature*, *436*(7050), 504-509, doi: 10.1038/nature03639.

Clark, B. C., et al. (2005), Chemistry and mineralogy of outcrops at Meridiani Planum, *Earth Planet Sc Lett*, *240*(1), 73-94, doi: 10.1016/j.epsl.2005.09.040.

Condie, K. C. (1993), Chemical Composition and Evolution of the Upper Continental-Crust: Contrasting Results from Surface Samples and Shales, *Chem.Geol.*, *104*(1-4), 1-37, doi: 10.1016/0009-2541(93)90140-E.

Cowan, C. A., and N. P. James (1992), Diastasis Cracks: mechanically generated synaeresis-like cracks in Upper Cambrian shallow water oolite and ribbon carbonates, *Sedimentology*, *39*(6), 1101-1118, doi: 10.1111/j.1365-3091.1992.tb01999.x.

Dehouck, E., S. M. McLennan, P. Y. Meslin, and A. Cousin (2014), Constraints on abundance, composition, and nature of X-ray amorphous components of soils and rocks at Gale crater, Mars, *Journal of Geophysical Research: Planets*, *119*(12), 2640-2657, doi: 10.1002/2014je004716.

Di Achille, G., and B. Hynek (2010), Ancient ocean on Mars supported by global distribution of deltas and valleys, *Nat Geosci*, *3*, 459-463, doi: 10.1038/ngeo89110.1038/NGEO891.

DiBiase, R. A., A. B. Limaye, J. S. Scheingross, W. W. Fischer, and M. P. Lamb (2013), Deltaic deposits at Aeolis Dorsa: Sedimentary evidence for a standing body of water on the northern plains of Mars, *Journal of Geophysical Research: Planets*, *118*(6), 1285-1302, doi: 10.1002/jgre.20100.

Dorobek, S. L. (1987), Petrography, geochemistry, and origin of burial diagenetic facies, Siluro-Devonian Helderberg Group (carbonate rocks), central Appalachians, *AAPG Bulletin*, *71*(5), 492-514.

Dreibus, G., and H. Wanke (1985), Mars, a Volatile-Rich Planet, *Meteoritics*, *20*(2), 367-381.

Driscoll, R., and R. Leinz (2005), Methods for synthesis of some jarosites. Techniques and Methods, pp. 9.

Duck, R. W. (1995), Subaqueous Shrinkage Cracks and Early Sediment Fabrics Preserved in Pleistocene Calcareous Concretions, *J Geol Soc London*, *152*, 151-156, doi: 10.1144/gsjgs.152.1.0151.

Edgett, K. S., et al. (2012), Curiosity's Mars Hand Lens Imager (MAHLI) Investigation, *Space Sci Rev*, *170*(1-4), 259-317, doi: 10.1007/s11214-012-9910-4.

Ehlmann, B. L., and J. F. Mustard (2012), An in-situ record of major environmental transitions on early Mars at Northeast Syrtis Major, *Geophys Res Lett*, *39*(11), doi: 10.1029/2012gl051594.

Ehlmann, B. L., and C. S. Edwards (2014), Mineralogy of the Martian Surface, *Annu Rev Earth Pl Sc*, *42*(1), 291-315, doi: 10.1146/annurev-earth-060313-055024.

Ehlmann, B. L., and J. Buz (2015), Mineralogy and fluvial history of the watersheds of Gale, Knobel, and Sharp craters: A regional context for the Mars Science Laboratory Curiosity's exploration, *Geophys Res Lett*, *42*(2), 264-273, doi: 10.1002/2014gl062553.

Ehlmann, B. L., J. F. Mustard, S. L. Murchie, J. P. Bibring, A. Meunier, A. A. Fraeman, and Y. Langevin (2011), Subsurface water and clay mineral formation during the early history of Mars, *Nature*, *479*(7371), 53-60, doi: 10.1038/nature10582.

Ehlmann, B. L., J. F. Mustard, C. I. Fassett, S. C. Schon, J. W. Head Iii, D. J. Des Marais, J. A. Grant, and S. L. Murchie (2008a), Clay minerals in delta deposits and organic preservation potential on Mars, *Nat Geosci*, *1*(6), 355-358, doi: 10.1038/ngeo207.

Ehlmann, B. L., et al. (2008b), Orbital identification of carbonate-bearing rocks on Mars, *Science*, *322*(5909), 1828-1832, doi: 10.1126/science.1164759.

Engel, A. E., S. P. Itson, C. G. Engel, D. M. Stickney, and E. J. Cray (1974), Crustal Evolution and Global Tectonics: A Petrogenic View, *Geological Society of America Bulletin*, *85*, 842-858.

Evamy, B. (1969), The precipitational environment and correlation of some calcite cements deduced from artificial staining, *Journal of Sedimentary Research*, *39*(2), 787-793.

Fairchild, I. J., G. Einsele, and T. R. Song (1997), Possible seismic origin of molar tooth structures in Neoproterozoic carbonate ramp deposits, north China, *Sedimentology*, *44*(4), 611-636, doi: 10.1046/j.1365-3091.1997.d01-40.x.

Falkowski, P. G., and Y. Isozaki (2008), The Story of O2, *Science*, *322*(5901), 540-542, doi: 10.1126/science.1162641.

Farley, K. A., et al. (2014), In Situ Radiometric and Exposure Age Dating of the Martian Surface, *Science*, *343*(6169), doi: 10.1126/science.1247166.

Fassett, C. I., and J. W. Head (2005), Fluvial sedimentary deposits on Mars: Ancient deltas in a crater lake in the Nili Fossae region, *Geophys Res Lett*, *32*(14), doi: 10.1029/2005gl023456.

Fedo, C. M., H. W. Nesbitt, and G. M. Young (1995), Unraveling the Effects of Potassium Metasomatism in Sedimentary-Rocks and Paleosols, with Implications for Paleoweathering Conditions and Provenance, *Geology; Geology*, *23*(10), 921-924, doi: 10.1130/0091-7613(1995)023<0921:Uteopm>2.3.Co;2.

Fedo, C. M., G. M. Grant, and H. W. Nesbitt (1997), Paleoclimatic control on the composition of the Paleoproterozoic Serpent Formation, Huronian Supergroup, Canada: a greenhouse to icehouse transition, *Precambrian Res*, *86*(3-4), 201-223, doi: 10.1016/S0301-9268(97)00049-1.

Fedo, C. M., K. N. Sircombe, and R. H. Rainbird (2003), Detrital Zircon Analysis of the Sedimentary Record, *Reviews in Mineralogy and Geochemistry*, *53*(1), 277-303, doi: 10.2113/0530277.

Fedo, C. M., I. O. McGlynn, and H. Y. McSween (2015), Grain size and hydrodynamic sorting controls on the composition of basaltic sediments: Implications for interpreting martian soils, *Earth Planet Sc Lett*, *423*, 67-77, doi: 10.1016/j.epsl.2015.03.052.

Fergason, R. L., P. R. Christensen, M. P. Golombek, and T. J. Parker (2012), Surface Properties of the Mars Science Laboratory Candidate Landing Sites: Characterization from Orbit and Predictions, *Space Sci Rev*, *170*(1-4), 739-773, doi: 10.1007/s11214-012-9891-3.

Ferguson, R., T. Hoey, S. Wathen, and A. Werritty (1996), Field evidence for rapid downstream fining of river gravels through selective transport, *Geology; Geology*, *24*(2), 179-182, doi: 10.1130/0091-7613(1996)024<0179:Fefrdf>2.3.Co;2.

Filiberto, J., and A. H. Treiman (2009), Martian magmas contained abundant chlorine, but little water, *Geology; Geology*, *37*(12), 1087-1090, doi: 10.1130/g30488a.1.

Fischer, W. F. (2016), pers. communication., edited.

Fraeman, A. A., et al. (2013), A hematite-bearing layer in Gale Crater, Mars: Mapping and implications for past aqueous conditions, *Geology; Geology*, *41*(10), 1103-1106, doi: 10.1130/g34613.1.

Frank, T. D., and T. W. Lyons (1998), "Molar-tooth" structures: A geochemical perspective on a Proterozoic enigma, *Geology; Geology*, *26*(8), 683-686, doi: 10.1130/0091-7613(1998)026<0683:Mtsagp>2.3.Co;2.

Frihy, O. E. (1994), Discrimination of Accreted and Eroded Coasts Using Heavy Mineral Compositions of the Nile Delta Beach Sands, Egypt, *Sedimentology*, *41*(5), 905-912, doi: 10.1111/j.1365-3091.1994.tb01431.x.

Frihy, O. E., M. F. Lotfy, and P. D. Komar (1995), Spatial Variations in Heavy Minerals and Patterns of Sediment Sorting Along the Nile Delta, Egypt, *Sedimentary Geology*, *97*(1-2), 33-41, doi: 10.1016/0037-0738(94)00135-H.

Furniss, G., J. F. Rittel, and D. Winston (1998), Gas bubble and expansion crack origin of "molar-tooth" calcite structures in the Middle Proterozoic Belt Supergroup, western Montana, *Journal of Sedimentary Research*, *68*(1), 104-114.

Garzanti, E., S. Andò, and G. Vezzoli (2008), Settling equivalence of detrital minerals and grain-size dependence of sediment composition, *Earth Planet Sc Lett*, *273*(1-2), 138-151, doi: 10.1016/j.epsl.2008.06.020.

Gast, P. W. (1968), Trace Element Fractionation and the Origin of Tholeiitic and Alkaline Magma Types, *Geochim Cosmochim Ac*, *32*, 1057-1086.

Gellert, R., and B. C. Clark (2015), In Situ Compositional Measurements of Rocks and Soils with the Alpha Particle X-ray Spectrometer on Nasa's Mars Rovers, *Elements*, *11*(1), 39-44, doi: 10.2113/gselements.11.1.39.

Gellert, R., J. L. Campbell, K. P. L., L. A. Leshin, G. W. Lugmair, J. G. Spray, S. W. Squyres, and A. S. Yen (2009), The Alpha-Particle-X-ray-Spectrometer (APXS) for the Mars Science Laboratory (MSL) Rover Mission, paper presented at 40th Lunar and Planetary Science Conference, LPI, Houston, TX, Abs. #2364.

Gellert, R., et al. (2006), Alpha Particle X-Ray Spectrometer (APXS): Results from Gusev crater and calibration report, *J Geophys Res*, *111*(E2), doi: 10.1029/2005je002555.

Golden, D. C., D. W. Ming, R. V. Morris, and S. A. Mertzman (2005), Laboratory-simulated acid-sulfate weathering of basaltic materials: Implications for formation of sulfates at Meridiani Planum and Gusev crater, Mars, *J Geophys Res*, *110*(E12), doi: 10.1029/2005je002451.

Goldspiel, J. M., and S. W. Squyres (1991), Ancient Aqueous Sedimentation on Mars, *Icarus*, *89*(2), 392-410, doi: 10.1016/0019-1035(91)90186-W.

Golombek, M. P., W. B. Banerdt, K. L. Tanaka, and D. M. Tralli (1992), A prediction of Mars seismicity from surface faulting, *Science*, *258*(5084), 979-981, doi: 10.1126/science.258.5084.979.

Gross, J., A. H. Treiman, J. Filiberto, and C. D. K. Herd (2011), Primitive olivine-phyric shergottite NWA 5789: Petrography, mineral chemistry, and cooling history imply a magma similar to Yamato-980459, *Meteoritics & Planetary Science*, no-no, doi: 10.1111/j.1945-5100.2010.01152.x.

Grotzinger, J., and R. Milliken (2012), *The Sedimentary Rock Record of Mars: Distribution, Origins, and Global Stratigraphy*.

Grotzinger, J., et al. (2005), Stratigraphy and sedimentology of a dry to wet eolian depositional system, Burns formation, Meridiani Planum, Mars, *Earth Planet Sc Lett*, *240*(1), 11-72, doi: 10.1016/j.epsl.2005.09.039.

Grotzinger, J., et al. (2012), Mars Science Laboratory Mission and Science Investigation, *Space Sci Rev*, *170*(1-4), 5-56, doi: 10.1007/s11214-012-9892-2.

Grotzinger, J. P., et al. (2015), Deposition, exhumation, and paleoclimate of an ancient lake deposit, Gale crater, Mars, *Science*, *350*(6257), aac7575, doi: 10.1126/science.aac7575.

Grotzinger, J. P., et al. (2014), A habitable fluvio-lacustrine environment at Yellowknife Bay, Gale crater, Mars, *Science*, *343*(6169), 1242777, doi: 10.1126/science.1242777.

Grover, G., and J. F. Read (1983), Paleoaquifer and Deep Burial Related Cements Defined by Regional Cathodoluminescent Patterns, Middle Ordovician Carbonates, Virginia, *Aapg Bull*, *67*(8), 1275-1303.

Halley, R. B., and J. W. Schmoker (1983), High-Porosity Cenozoic Carbonate Rocks of South Florida - Progressive Loss of Porosity with Depth, *Aapg Bull*, *67*(2), 191-200.

Hartmann, W. K., and G. Neukum (2001), Cratering Chronology and the Evolution of Mars, *Space Sci Rev*, *96*(1-4), 165-194, doi: 10.1023/A:1011945222010.

Head, J. W., H. Hiesinger, M. A. Ivanov, M. A. Kreslavsky, S. Pratt, and B. J. Thomson (1999), Possible Ancient Oceans on Mars: Evidence from Mars Orbiter Laser Altimeter Data, *Science*, *286*(5447), 2134-2137, doi: 10.1126/science.286.5447.2134.

Hodges, K. V. (2005), 40Ar/39Ar Thermochronology of Detrital Minerals, *Reviews in Mineralogy and Geochemistry*, *58*(1), 239-257, doi: 10.2138/rmg.2005.58.9.

Hoek, J. D. (1991), A classification of dyke-fracture geometry with examples from Precambrian dyke swarms in the Vestfold Hills, Antarctica, *Geologische-Rundschau*, *80*(2), 233-248, doi: 10.1007/Bf01829363.

Horodyski, R. J. (1976), Stromatolites of the upper Siyeh limestone (middle proterozoic), belt supergroup, Glacier National Park, Montana, *Precambrian Res*, *3*(6), 517-536.

Hughes, M. G., J. B. Keene, and R. G. Joseph (2000), Hydraulic sorting of heavy-mineral grains by swash on a medium-sand beach, *Journal of Sedimentary Research*, *70*(5), 994-1004, doi: 10.1306/112599700994.

Hurowitz, J., et al. (2016), Dynamic Geochemical Conditions Recorded by Lakebed Mudstones in Gale Crater, Mars, paper presented at 47th Lunar and Planetary Science Conference, LPI, Houston, TX, Abs. #1751.

Hurowitz, J. A., W. W. Fischer, N. J. Tosca, and R. E. Milliken (2010), Origin of acidic surface waters and the evolution of atmospheric chemistry on early Mars, *Nat Geosci*, *3*(5), 323-326, doi: 10.1038/ngeo831.

Jakosky, B. M. (1991), Mars Volatile Evolution - Evidence from Stable Isotopes, *Icarus*, *94*(1), 14-31, doi: 10.1016/0019-1035(91)90138-J.

Jambor, J. L., D. K. Nordstrom, and C. N. Alpers (2000), Metal-sulfate Salts from Sulfide Mineral Oxidation, *Reviews in Mineralogy and Geochemistry*, *40*(1), 303-350, doi: 10.2138/rmg.2000.40.6.

James, N. P., G. M. Narbonne, and A. G. Sherman (1998), Molar-tooth carbonates: Shallow subtidal facies of the mid- to late Proterozoic, *Journal of Sedimentary Research*, *68*(5), 716-722.

Jerolmack, D. J., and D. Mohrig (2007), Conditions for branching in depositional rivers, *Geology; Geology*, *35*(5), 463-466, doi: 10.1130/G23308a.1.

Jerolmack, D. J., D. Mohrig, M. T. Zuber, and S. Byrne (2004), A minimum time for the formation of Holden Northeast fan, Mars, *Geophys Res Lett*, *31*(21), doi: 10.1029/2004gl021326.

Johnsson, M. J., and A. Basu (1993), *Processes controlling the composition of clastic sediments*, Geological Society of America.

Kah, L. C., R. E. Kroynak, D. W. Ming, J. P. Grotzinger, J. Schieber, D. Sumner, and K. Edgett (2015), Diagenetic Crystal Growth in the Murray Formation, Gale Crater, Mars, paper presented at Geological Society of America Baltimore, MD, 267.

Kaufman, J., H. S. Cander, L. D. Daniels, and W. J. Meyers (1988), Calcite Cement Stratigraphy and Cementation History of the Burlington-Keokuk Formation (Mississippian), Illinois and Missouri, *Journal of Sedimentary Petrology*, *58*(2), 312-326.

Kirk, R. L., et al. (2008), Ultrahigh resolution topographic mapping of Mars with MRO HiRISE stereo images: Meter-scale slopes of candidate Phoenix landing sites, *J Geophys Res*, *113*, doi: 10.1029/2007je003000.

Kite, E. S., K. W. Lewis, M. P. Lamb, C. E. Newman, and M. I. Richardson (2013), Growth and form of the mound in Gale Crater, Mars: Slope wind enhanced erosion and transport, *Geology; Geology*, *41*(5), 543-546, doi: 10.1130/G33909.1.

Knipe, R. (1992), Faulting processes and fault seal, *Structural and tectonic modelling and its application to petroleum geology: Norwegian Petroleum Society Special Publication*, *1*, 325-342.

Knoll, A. H., and J. Grotzinger (2006), Water on Mars and the prospect of Martian life, *Elements*, *2*(3), 169-173, doi: 10.2113/gselements.2.3.169.

Komar, P. D. (2007), The Entrainment, Transport, and Sorting of Heavy Minerals by Waves and Currents, in *Heavy Minerals in Use*, edited by M. T. Mange and D. T. Wright, pp. 3-48, Elsevier, Italy.

Kroynak, R. E., L. C. Kah, J. P. Grotzinger, M. Fisk, D. Sumner, M. Nachon, N. Mangold, D. Blaney, W. Rapin, and R. Wiens (2015), Garden City: A complex vein system observed by the Curiosity rover at Pahrump Hills, Gale Crater, Mars, paper presented at Geological Society of America, Baltimore, MD, 217.

Kuhlmann, G., P. L. de Boer, R. B. Pedersen, and T. E. Wong (2004), Provenance of Pliocene sediments and paleoenvironmental changes in the southern North Sea region using Samarium–Neodymium (Sm/Nd) provenance ages and clay mineralogy, *Sedimentary Geology*, *171*(1-4), 205-226, doi: 10.1016/j.sedgeo.2004.05.016.

Lachenbruch, A. H. (1962), Mechanics of thermal contraction cracks and ice-wedge polygons in permafrost, *Geological Society of America Special Papers*, *70*, 1-66.

Lachenbruch, A. H. (1963), Contraction Theory of Ice-Wedge Polygons: A Qualitative Discussion, in *Permafrost International Conference*, edited, pp. 63-70, National Academy of Sciences, Lafayette, Indiana.

Langmuir, C. H., R. D. Vocke, G. N. Hanson, and S. R. Hart (1978), A General Mixing Equation with Applications to Icelandic Basalts, *Earth Planet Sc Lett*, *37*, 380-392.

Lanza, N. L., et al. (submitted), Oxidation of Manganese in an Ancient Aquifer, Kimberley Formation, Gale Crater, Mars, *Nature*.

Lasue, J., et al. (2016), Observation of > 5 wt % zinc at the Kimberley outcrop, Gale crater, Mars, *Journal of Geophysical Research: Planets*, *121*(3), 338-352, doi: 10.1002/2015je004946.

Léveillé, R. J., et al. (2014), Chemistry of fracture-filling raised ridges in Yellowknife Bay, Gale Crater: Window into past aqueous activity and habitability on Mars, *J Geophys Res-Planet*, *119*(11), 2398-2415, doi: 10.1002/2014je004620.

Long, J. C. S., et al. (1996), *Rock Fractures and Fluid Flow: Contemporary Understanding and Applications*, 551 pp., National Academy Press, Washington, D. C.

Longman, M. W. (1980), Carbonate Diagenetic Textures from Nearsurface Diagenetic Environments, *Aapg Bull*, *64*(4), 461-487.

Mackie, W. (1923), The Principles that Regulate the Distribution of Particles of Heavy Minerals in Sedimentary Rocks, as illustrated by the Sandstones of the North-East of Scotland, *Trans. Edinburgh Geol. Soc.*, *11*, 138-164.

Maki, J., D. Thiessen, A. Pourangi, P. Kobzeff, T. Litwin, L. Scherr, S. Elliott, A. Dingizian, and M. Maimone (2012), The Mars Science Laboratory Engineering Cameras, *Space Sci Rev*, *170*(1-4), 77-93, doi: 10.1007/s11214-012-9882-4.

Malin, M., M. Caplinger, K. Edgett, F. Ghaemi, M. Ravine, J. Schaffner, J. Baker, J. Bardis, D. DiBiase, and J. Maki (2010), The Mars Science Laboratory (MSL) mast-mounted cameras (Mastcams) flight instruments, paper presented at 41st Lunar and Planetary Science Conference, LPI, Houston, TX, Abs. #1123.

Malin, M. C., and K. S. Edgett (2000), Sedimentary rocks of early Mars, *Science*, *290*(5498), 1927-1937, doi: 10.1126/science.290.5498.1927.

Malin, M. C., and K. S. Edgett (2003), Evidence for persistent flow and aqueous sedimentation on early Mars, *Science*, *302*(5652), 1931-1934, doi: 10.1126/science.1090544.

Manda, A. K., and M. R. Gross (2006), Estimating aquifer-scale porosity and the REV for karst limestones using GIS-based spatial analysis, *Geol S Am S*, *404*, 177-189, doi: 10.1130/2006.2404(15).

Mangold, N., D. Baratoux, O. Arnalds, J. M. Bardintzeff, B. Platevoet, M. Grégoire, and P. Pinet (2011), Segregation of olivine grains in volcanic sands in Iceland and implications for Mars, *Earth Planet Sc Lett*, *310*(3-4), 233-243, doi: 10.1016/j.epsl.2011.07.025.

Mangold, N., et al. (2016), Composition of conglomerates analyzed by the Curiosity rover: Implications for Gale Crater crust and sediment sources, *J Geophys Res-Planet*, *121*(3), 353-387, doi: 10.1002/2015je004977.

Marshall, D., and C. D. Anglin (2004), CO2-clathrate destabilization: a new model of formation for molar tooth structures, *Precambrian Res*, *129*(3-4), 325-341, doi: 10.1016/j.precamres.2003.10.007.

Mattson, S., R. Kirk, R. Heyd, A. McEwen, E. Eliason, T. Hare, R. Beyer, E. Howington-Kraus, C. H. Okubo, and K. Herkenhoff (2011), Release of HiRISE Digital Terrain Models to the Planetary Data System, paper presented at 42nd Lunar and Planetary Science Conference, LPI, Houston, TX, Abs. #1558.

McCauley, J. F. (1973), Mariner 9 evidence for wind erosion in the equatorial and mid-latitude regions of Mars, *J Geophys Res*, *78*(20), 4123-4137, doi: 10.1029/JB078i020p04123.

McCauley, J. F., M. H. Carr, J. A. Cutts, W. K. Hartmann, H. Masursky, D. J. Milton, R. P. Sharp, and D. E. Wilhelms (1972), Preliminary Mariner 9 report on the geology of Mars, *Icarus*, *17*(2), 289-327.

McEwen, A. S., et al. (2007a), Mars Reconnaissance Orbiter's High Resolution Imaging Science Experiment (HiRISE), *J Geophys Res*, *112*(E5), doi: 10.1029/2005je002605.

McEwen, A. S., et al. (2007b), A closer look at water-related geologic activity on Mars, *Science*, *317*(5845), 1706-1709, doi: 10.1126/science.1143987.

McLennan, S., and J. Grotzinger (2008a), The sedimentary rock cycle of Mars, *The Martian Surface-Composition, Mineralogy, and Physical Properties*, *1*, 541.

McLennan, S. M. (2001), Relationships between the trace element composition of sedimentary rocks and upper continental crust, *Geochemistry Geophysics Geosystems*, *2*.

McLennan, S. M. (2012), Geochemistry of Sedimentary Processes on Mars, in *Sedimentary Geology of Mars*, edited by J. Grotzinger and R. Milliken, p. 270, SEPM, Tulsa, Oklahoma.

McLennan, S. M., and J. Grotzinger (2008b), The Sedimentary Rock Cycle of Mars, in *The Martian Surface: Composition, Mineralogy, and Physical Properties*, edited by J. F. Bell, pp. 541-577, Cambridge University Press.

McLennan, S. M., S. R. Taylor, M. T. McCulloch, and J. B. Maynard (1990), Geochemical and Nd-Sr Isotopic Composition of Deep-Sea Turbidites - Crustal Evolution and Plate Tectonic Associations, *Geochim Cosmochim Ac*, *54*(7), 2015-2050, doi: 10.1016/0016-7037(90)90269-Q.

McLennan, S. M., S. Hemming, D. K. McDaniel, and G. N. Hansen (1993), Geochemical approaches to sedimentation, provenance, and tectonics, *Geological Society of America Special Papers*, *284*, 21-40, doi: 10.1130/SPE284-p21.

McLennan, S. M., B. Bock, S. R. Hemming, J. A. Hurowitz, S. M. Lev, and D. K. McDaniel (2003), The roles of provenance and sedimentary processes in the geochemistry of sedimentary rocks, in *Geochemistry of Sediments and Sedimentary Rocks: Evolutionary Considerations to Mineral Deposit-Forming Environments*, edited by D. R. Lentz, pp. 7-38, Geological Association of Canada: GeoText.

McLennan, S. M., E. Dehouck, J. P. Grotzinger, J. A. Hurowitz, N. Mangold, and K. Siebach (2015), Geochemical Record of Open-System Chemical Weathering at Gale Crater and Implications for Paleoclimates on Mars, paper presented at 46th Lunar and Planetary Science Conference, LPI, Houston, TX, Abs. #2533.

McLennan, S. M., et al. (2005), Provenance and diagenesis of the evaporite-bearing Burns formation, Meridiani Planum, Mars, *Earth Planet Sc Lett*, *240*(1), 95-121, doi: 10.1016/j.epsl.2005.09.041.

McLennan, S. M., et al. (2014), Elemental Geochemistry of Sedimentary Rocks at Yellowknife Bay, Gale Crater, Mars, *Science*, *343*(6169), doi: 10.1126/science.1244734.

Meyers, W. J. (1974), Carbonate cement stratigraphy of the Lake Valley Formation (Mississippian) Sacramento Mountains, New Mexico, *Journal of Sedimentary Research*, *44*(3), 837-861.

Meyers, W. J. (1991), Calcite cement stratigraphy: an overview. SEPM Short Course, 25, pp. 133-148.

Meyers, W. J., and K. C. Lohmann (1985), Isotope geochemistry of regionally extensive calcite cement zones and marine components in Mississippian limestones, New Mexico, in *Carbonate Cements*, edited by N. Schneidermann and P. M. Harris, pp. 223-239, Soc. Econ. Pal. Min. Sp. Pub. 36.

Milliken, R. E., J. P. Grotzinger, and B. J. Thomson (2010), Paleoclimate of Mars as captured by the stratigraphic record in Gale Crater, *Geophys Res Lett*, *37*(4), doi: 10.1029/2009gl041870.

Ming, D. W., et al. (2014), Volatile and Organic Compositions of Sedimentary Rocks in Yellowknife Bay, Gale Crater, Mars, *Science*, *343*(6169), doi: 10.1126/science.1245267.

Mitchener, H., and H. Torfs (1996), Erosion of mud/sand mixtures, *Coastal Engineering*, *29*(1–2), 1-25, doi: 10.1016/S0378-3839(96)00002-6.

Moratto, Z., M. Broxton, R. Beyer, M. Lundy, and K. Husmann (2010), Ames Stereo Pipeline, NASA's open source automated stereogrammetry software, paper presented at 41st Lunar and Planetary Science Conference, LPI, Houston, TX, Abs. #2364.

Morris, R., et al. (2014), The Amorphous Component in Martian Basaltic Soil in Global Perspective from MSL and MER Missions, paper presented at 45th Lunar and Planetary Science Conference, LPI, Houston, TX, Abs. #1319.

Morris, R. V., et al. (submitted), Silicic volcanism on Mars evidenced by tridymite in high-SiO2 sedimentary rock at Gale crater, *PNAS*.

Morrison, S. M., et al. (2015), Crystal-Chemical Analysis of Martian Minerals in Gale Crater, paper presented at 46th Lunar and Planetary Science Conference, LPI, Houston, Abs. #2506.

Murchie, S. L., et al. (2009), A synthesis of Martian aqueous mineralogy after 1 Mars year of observations from the Mars Reconnaissance Orbiter, *J Geophys Res*, *114*, doi: 10.1029/2009je003342.

Murray, B. C., L. A. Soderblom, J. A. Cutts, R. P. Sharp, D. J. Milton, and R. B. Leighton (1972), Geological Framework of the South Polar Region of Mars, *Icarus*, *17*(2), 328-345.

Mustard, J. F., F. Poulet, B. L. Ehlmann, R. Milliken, and A. Fraeman (2012), Sequestration of Volatiles in the Martian Crust through Hydrated Minerals: A Significant Planetary Reservoir of Water, paper presented at 43rd Lunar and Planetary Science Conference, LPI, Houston, TX, Abs. #1539.

Mustard, J. F., et al. (2008), Hydrated silicate minerals on Mars observed by the Mars Reconnaissance Orbiter CRISM instrument, *Nature*, *454*(7202), 305-309, doi: 10.1038/nature07097.

Nachon, M., et al. (2014), Calcium sulfate veins characterized by ChemCam/Curiosity at Gale crater, Mars, *J Geophys Res-Planet*, *119*(9), 1991-2016, doi: 10.1002/2013je004588.

NASA-JPL (2013), Mars Science Laboratory Project Software Interface Specification (SIS), Mast Camera (Mastcam), Mars Hand Lens Imager (MAHLI), and Mars Descent

Imager (MARDI) Experiment Data Record (EDR) and Reduced Data Record (RDR) PDS Data Products, edited.

Nelson, E. P., A. J. Kullman, M. H. Gardner, and M. Batzle (1999), Fault-Fracture Networks and Related Fluid Flow and Sealing, Brushy Canyon Formation, West Texas, in *Faults and Subsurface Fluid Flow in the Shallow Crust*, edited by W. C. Haneburg, P. S. Mozley, J. C. Moore and L. B. Goodwin, pp. 69-81, American Geophysical Union.

Nesbitt, H. W. (2003), Petrogenesis of siliciclastic sediments and sedimentary rocks, in *Geochemistry of Sediments and Sedimentary Rocks: Evolutionary Considerations to Mineral Deposit-Forming Environments*, edited by D. R. Lentz, pp. 39-51, Geological Association of Canada.

Nesbitt, H. W., and G. M. Young (1982), Early Proterozoic Climates and Plate Motions Inferred from Major Element Chemistry of Lutites, *Nature*, *299*(5885), 715-717, doi: 10.1038/299715a0.

Nesbitt, H. W., and G. M. Young (1984), Prediction of Some Weathering Trends of Plutonic and Volcanic-Rocks Based on Thermodynamic and Kinetic Considerations, *Geochim Cosmochim Ac*, *48*(7), 1523-1534, doi: 10.1016/0016-7037(84)90408-3.

Nesbitt, H. W., and R. E. Wilson (1992), Recent Chemical Weathering of Basalts, *American Journal of Science*, *292*(10), 740-777.

Nesbitt, H. W., and G. M. Young (1996), Petrogenesis of sediments in the absence of chemical weathering: Effects of abrasion and sorting on bulk composition and mineralogy, *Sedimentology*, *43*(2), 341-358, doi: 10.1046/j.1365-3091.1996.d01-12.x.

Nesbitt, H. W., G. M. Young, S. M. McLennan, and R. R. Keays (1996), Effects of Chemical Weathering and Sorting on the Petrogenesis of Siliciclastic Sediments, with Implications for Provenance Studies, *The Journal of Geology*, *104*(5), 525-542, doi: 10.1086/629850.

Newsom, H. E., et al. (2016), The Materials at an Unconformity between the Murray and Stimson Formations at Marias Pass, Gale Crater, Mars, paper presented at 47th Lunar and Planetary Science Conference LPI, Houston, TX, Abs. #2397.

O'Brien, N. R. (1996), Shale lamination and sedimentary processes, *Geological Society, London, Special Publications*, *116*(1), 23-26, doi: 10.1144/GSL.SP.1996.116.01.04.

O'Connor, M. P. (1972), Classification and Environmental Interpretation of the Cryptalgal Organosedimentary "MolarTooth" Structure from the Late Precambrian Belt-Purcell Supergroup, *The Journal of Geology*, *80*(5), 592-610.

Ohta, T. (2004), Geochemistry of Jurassic to earliest Cretaceous deposits in the Nagato Basin, SW Japan: implication of factor analysis to sorting effects and provenance signatures, *Sedimentary Geology*, *171*(1-4), 159-180, doi: 10.1016/j.sedgeo.2004.05.014.

Okubo, C. H., and A. S. McEwen (2007), Fracture-controlled paleo-fluid flow in Candor Chasma, Mars, *Science*, *315*(5814), 983-985, doi: 10.1126/science.1136855.

Olson, J. E., S. E. Laubach, and R. H. Lander (2009), Natural fracture characterization in tight gas sandstones: Integrating mechanics and diagenesis, *AAPG Bulletin*, *93*(11), 1535-1549, doi: 10.1306/08110909100.

Palmer, M. R., and J. M. Edmond (1989), The strontium isotope budget of the modern ocean, *Earth Planet Sc Lett*, *92*(1), 11-26, doi: 10.1016/0012-821x(89)90017-4.

Palucis, M. C., W. E. Dietrich, A. G. Hayes, R. M. E. Williams, S. Gupta, N. Mangold, H. Newsom, C. Hardgrove, F. Calef, and D. Y. Sumner (2014), The origin and evolution of the Peace Vallis fan system that drains to the Curiosity landing area, Gale Crater, Mars, *J Geophys Res-Planet*, *119*(4), 705-728, doi: 10.1002/2013je004583.

Papike, J. J., J. M. Karner, C. K. Shearer, and P. V. Burger (2009), Silicate mineralogy of martian meteorites, *Geochim Cosmochim Ac*, *73*(24), 7443-7485, doi: 10.1016/j.gca.2009.09.008.

Parker, T. J., M. C. Malin, F. J. Calef, R. G. Deen, H. E. Gengl, M. P. Golombek, J. R. Hall, O. Pariser, M. Powell, and R. S. Sletten (2013), Localization and 'Contextualization' of Curiosity in Gale Crater, and Other Landed Mars Missions, paper presented at 44th Lunar and Planetary Science Conference, LPI, Houston, TX, Abs. #2534.

Peck, D. L., and T. Minakami (1968), The formation of columnar joints in the upper part of Kilauean lava lakes, Hawaii, *GSA Bulletin*, *79*(9), 1151-1166.

Pettijohn, F. J., and P. E. Potter (1964), *Atlas and glossary of primary sedimentary structures*, 370 pp., Springer-Verlag New York, Germany.

Plaut, J. J., et al. (2007), Subsurface radar sounding of the south polar layered deposits of Mars, *Science*, *316*(5821), 92-95, doi: 10.1126/science.1139672.

Plummer, P. S., and V. A. Gostin (1981), Shrinkage Cracks - Desiccation or Synaeresis, *Journal of Sedimentary Petrology*, *51*(4), 1147-1156.

Pollock, M. D., L. C. Kah, and J. K. Bartley (2006), Morphology of Molar-Tooth Structures in Precambrian Carbonates: Influence of Substrate Rheology and Implications for Genesis, *Journal of Sedimentary Research*, *76*(2), 310-323, doi: 10.2110/jsr.2006.021.

Poulet, F., et al. (2005), Phyllosilicates on Mars and implications for early martian climate, *Nature*, *438*(7068), 623-627, doi: 10.1038/nature04274.

Pratt, B. R. (1998a), Molar-tooth structure in Proterozoic carbonate rocks: Origin from synsedimentary earthquakes, and implications for the nature and evolution of basins and marine sediment, *Geological Society of America Bulletin*, *110*(8), 1028-1045, doi: 10.1130/0016-7606(1998)110<1028:Mtsipc>2.3.Co;2.

Pratt, B. R. (1998b), Syneresis cracks: subaqueous shrinkage in argillaceous sediments caused by earthquake-induced dewatering, *Sedimentary Geology*, *117*(1-2), 1-10, doi: 10.1016/S0037-0738(98)00023-2.

Press, W. H., S. A. Teukolsky, W. T. Vetterling, and B. P. Flannery (1992), *Numerical Recipes in FORTRAN: The Art of Scientific Computing*, 2nd ed., 963 pp., Cambridge University Press, Cambridge.

Rampe, E., et al. (2016), Diagenesis in the Murray Formation, Gale Crater, Mars, paper presented at 47th Lunar and Planetary Science Conference, LPI, Houston, TX, Abs. #2543.

Rampe, E. B., et al. (in prep.), Mineralogical trends in mudstones from the Murray formation, Gale crater, Mars.

Ramseyer, K., J. E. Amthor, A. Matter, T. Pettke, M. Wille, and A. E. Fallick (2013), Primary silica precipitate at the Precambrian/Cambrian boundary in the South Oman Salt Basin, Sultanate of Oman, *Marine and Petroleum Geology*, *39*(1), 187-197, doi: 10.1016/j.marpetgeo.2012.08.006.

Reid, M. J., A. J. Gancarz, and A. L. Albee (1973), Constrained Least-Squares Analysis of Petrologic Problems with an Application to Lunar Sample 12040, *Earth Planet Sc Lett*, *17*(2), 433-445, doi: 10.1016/0012-821x(73)90212-4.

Rieder, R., T. Economou, H. Wanke, A. Turkevich, J. Crisp, J. Bruckner, G. Dreibus, and H. Y. McSween (1997), The Chemical Composition of Martian Soil and Rocks Returned by the Mobile Alpha Particle X-ray Spectrometer: Preliminary Results from the X-ray Mode, *Science*, *278*, 1771.

Rodriguez-Navarro, C. (1998), Evidence of honeycomb weathering on Mars, *Geophys Res Lett*, *25*(17), 3249-3252, doi: 10.1029/98gl02569.

Rubey, W. W. (1933), The size-distribution of heavy minerals within a water-laid sandstone, *Journal of Sedimentary Petrology*, *3*(1), 3-29.

Russell, R. D. (1937), Mineral composition of Mississippi River sands, *Bulletin of the Geological Society of America*, *48*(9/12), 1307-1348.

Santos, A. R., C. B. Agee, F. M. McCubbin, C. K. Shearer, P. V. Burger, R. Tartèse, and M. Anand (2015), Petrology of igneous clasts in Northwest Africa 7034: Implications for the petrologic diversity of the martian crust, *Geochim Cosmochim Ac*, *157*, 56-85, doi: 10.1016/j.gca.2015.02.023.

Sarbas, B., and U. Nohl (2008), The GEOROC database as part of a growing geoinformatics network, in *Geoinformatics 2008-Data to Knowledge, Proceedings: U.S. Geological Survey Scientific Investigations Report 2008*, edited by S. R. Brady, A. K. Sinha and L. C. Gundersen, pp. 42-43.

Sautter, V., et al. (2016), Magmatic complexity on early Mars as seen through a combination of orbital, in-situ and meteorite data, *Lithos*, *254-255*, 36-52, doi: 10.1016/j.lithos.2016.02.023.

Sautter, V., et al. (2015), In situ evidence for continental crust on early Mars, *Nat Geosci*, *8*(8), 605-609, doi: 10.1038/ngeo2474.

Schieber, J., S. Gupta, J. Grotzinger, and R. Suarez-Rivera (2013), Hydraulic Fracturing of Martian Mudstones, paper presented at Geological Society of America, Denver, CO, 39.

Schmidt, M. E., et al. (2014), Geochemical diversity in first rocks examined by the Curiosity Rover in Gale Crater: Evidence for and significance of an alkali and volatile-rich igneous source, *Journal of Geophysical Research: Planets*, *119*(1), 64-81, doi: 10.1002/2013je004481.

Schnurrenberger, D., J. Russell, and K. Kelts (2003), Classification of lacustrine sediments based on sedimentary components, *Journal of Paleolimnology*, *29*(2), 141-154, doi: 10.1023/A:1023270324800.

Sharp, R. P., and M. C. Malin (1975), Channels on Mars, *Geological Society of America Bulletin*, *86*(5), 593-609, doi: 10.1130/0016-7606(1975)86<593:Com>2.0.Co;2.

Sheldon, N. D. (2003), Pedogenesis and geochemical alteration of the Picture Gorge subgroup, Columbia River Basalt, Oregon, *Geological Society of America Bulletin*, *115*(11), 1377-1387, doi: 10.1130/B25223.1.

Shorlin, K. A., J. R. de Bruyn, M. Graham, and S. W. Morris (2000), Development and geometry of isotropic and directional shrinkage-crack patterns, *Physical Review E*, *61*(6), 6950-6957.

Siebach, K. L., and J. P. Grotzinger (2014a), Volumetric estimates of ancient water on Mount Sharp based on boxwork deposits, Gale Crater, Mars, *Journal of Geophysical Research: Planets*, *119*(1), 189-198, doi: 10.1002/2013je004508.

Siebach, K. L., and J. P. Grotzinger (2014b), Characterizing Sandstone Porosity along Curiosity's Traverse using MAHLI Imagery, paper presented at Eighth International Conference on Mars, Pasadena, CA, 1466.

Siebach, K. L., M. B. Baker, J. P. Grotzinger, S. M. McLennan, R. Gellert, and J. A. Hurowitz (in prep.), Sorting out Compositional Trends in Sedimentary Rocks of the Bradbury Group (Aeolus Palus), Gale Crater, Mars, *J Geophys Res*.

Siebach, K. L., J. P. Grotzinger, L. C. Kah, K. M. Stack, M. Malin, R. Leveille, and D. Y. Sumner (2014), Subaqueous shrinkage cracks in the Sheepbed mudstone: Implications for early fluid diagenesis, Gale crater, Mars, *J Geophys Res-Planet*, *119*(7), 1597-1613, doi: 10.1002/2014je004623.

Slatt, R. M., and N. Eyles (1981), Petrology of Glacial Sand - Implications for the Origin and Mechanical Durability of Lithic Fragments, *Sedimentology*, *28*(2), 171-183, doi: 10.1111/j.1365-3091.1981.tb01675.x.

Sletten, R. S., B. Hallet, and R. C. Fletcher (2003), Resurfacing time of terrestrial surfaces by the formation and maturation of polygonal patterned ground, *J Geophys Res*, *108*(E4), doi: 10.1029/2002je001914.

Slingerland, R. L. (1977), The Effects of Entrainment on the Hydraulic Equivalence Relationships of Light and Heavy Minerals, *Journal of Sedimentary Petrology*, *47*, 753-770.

Smith, A. G. (1968), The Origin and Deformation of Some "Molar-Tooth" Structures in the Precambrian BeltPurcell Supergroup, *The Journal of Geology*, *76*(4), 426-443.

Smith, D. E., G. A. Neumann, R. E. Arvidson, E. Guinness, and S. Slavney (2003), Mars Global Surveyor laser altimeter initial experiment gridded data record (MGS-M-MOLA), 5-MEGDR-L3-V1.0, edited, NASA Planetary Data System (PDS), Greenbelt, MD.

Soderblom, L. A., M. C. Malin, J. A. Cutts, and B. C. Murray (1973), Mariner 9 observations of the surface of Mars in the north polar region, *J Geophys Res*, *78*(20), 4197-4210, doi: 10.1029/JB078i020p04197.

Squyres, S. W., et al. (2004), In situ evidence for an ancient aqueous environment at Meridiani Planum, Mars, *Science*, *306*(5702), 1709-1714, doi: 10.1126/science.1104559.

Stack, K. M., et al. (2014), Diagenetic origin of nodules in the Sheepbed member, Yellowknife Bay formation, Gale crater, Mars, *J Geophys Res-Planet*, *119*(7), 1637-1664, doi: 10.1002/2014je004617.

Stolper, E. M., et al. (2013), The petrochemistry of Jake_M: a martian mugearite, *Science*, *341*(6153), 1239463, doi: 10.1126/science.1239463.

Stumm, W., and J. J. Morgan (2012), *Aquatic chemistry: chemical equilibria and rates in natural waters*, John Wiley & Sons.

Szabo, T., G. Domokos, J. P. Grotzinger, and D. J. Jerolmack (2015), Reconstructing the transport history of pebbles on Mars, *Nature communications*, *6*, 8366, doi: 10.1038/ncomms9366.

Tanaka, K. L., J. A. Skinner, J. M. Dohm, R. P. Irwin, E. J. Kolb, C. M. Fortezzo, T. Platz, G. G. Michael, and T. M. Hare (2014), Geologic map of Mars, doi: 10.3133/sim3292.

Taylor, S. M., and S. M. McLennan (2009), *Planetary Crusts: Their Composition, Origin, and Evolution*, Cambridge University Press.

Taylor, S. R., and S. M. McLennan (1995), The Geochemical Evolution of the Continental-Crust, *Rev Geophys*, *33*(2), 241-265, doi: 10.1029/95rg00262.

Team, R. (1997), Characterization of the Martian Surface Deposits by the Mars Pathfinder Rover, Sojourner, *Science*, *278*(5344), 1765-1768, doi: 10.1126/science.278.5344.1765.

Terzaghi, K. (1944), *Theoretical Soil Mechanics*, 510 pp., London.

Therriault, A. M., A. D. Fowler, and R. A. F. Grieve (2002), The Sudbury Igneous Complex: A Differentiated Impact Melt Sheet, *Economic Geology*, *97*(7), 1521-1540, doi: 10.2113/gsecongeo.97.7.1521.

Thomson, B. J., and N. Bridges (2008), Gale Crater: Context and layer diversity from HiRISE Images, paper presented at Third Mars Science Laboratory Landing Site Workshop, Monrovia, CA.

Thomson, B. J., N. T. Bridges, R. Milliken, A. Baldridge, S. J. Hook, J. K. Crowley, G. M. Marion, C. R. de Souza, A. J. Brown, and C. M. Weitz (2011), Constraints on the origin and evolution of the layered mound in Gale Crater, Mars using Mars Reconnaissance Orbiter data, *Icarus*, *214*(2), 413-432, doi: 10.1016/j.icarus.2011.05.002.

Tosca, N. J. (2004), Acid-sulfate weathering of synthetic Martian basalt: The acid fog model revisited, *J Geophys Res*, *109*(E5), doi: 10.1029/2003je002218.

Tosca, N. J., A. H. Knoll, and S. M. McLennan (2008), Water activity and the challenge for life on early Mars, *Science*, *320*(5880), 1204-1207, doi: 10.1126/science.1155432.

Tosca, N. J., F. A. Macdonald, J. V. Strauss, D. T. Johnston, and A. H. Knoll (2011), Sedimentary talc in Neoproterozoic carbonate successions, *Earth Planet Sc Lett*, *306*(1-2), 11-22, doi: 10.1016/j.epsl.2011.03.041.

Treiman, A. H., et al. (2015), Mineralogy, Provenance, and Diagenesis of a Potassic Basaltic Sandstone on Mars: CheMin X-ray Diffraction of the Windjana Sample (Kimberley Area, Gale Crater), *Journal of Geophysical Research: Planets*, doi: 10.1002/2015je004932.

Tucker, E. (2009), *Sedimentary Petrology: An Introduction to the Origin of Sedimentary Rocks*, Wiley.

VanBommel, S. J., R. Gellert, J. A. Berger, J. L. Campbell, L. M. Thompson, K. S. Edgett, M. J. McBride, M. E. Minitti, I. Pradler, and N. I. Boyd (2016), Deconvolution of distinct lithology chemistry through oversampling with the Mars Science Laboratory Alpha Particle X-Ray Spectrometer, *X-Ray Spectrometry*, *45*(3), 155-161, doi: 10.1002/xrs.2681.

Vaniman, D., et al. (2014), Mineralogy of a Mudstone at Yellowknife Bay, Gale Crater, Mars, *Science*, *343*(6169), doi: 10.1126/science.1243480.

Vaniman, D. T., D. L. Bish, S. J. Chipera, C. I. Fialips, J. W. Carey, and W. C. Feldman (2004), Magnesium sulphate salts and the history of water on Mars, *Nature*, *431*(7009), 663-665, doi: 10.1038/nature02973.

Vervott, J. D., P. J. Patchett, J. Blichert-Toft, and F. Albarede (1999), Relationships between Lu-Hf and Sm-Nd isotopic systems in the global sedimentary system, *Earth Planet Sc Lett*, *168*, 79-99.

Vezzoli, G., E. Garzanti, and S. Monguzzi (2004), Erosion in the Western Alps (Dora Baltea basin) 1. Quantifying Sediment Provenance, *Sedimentary Geology*, *171*(1-4), 227-246, doi: 10.1016/j.sedgeo.2004.05.017.

von Eynatten, H. (2004), Statistical modelling of compositional trends in sediments, *Sedimentary Geology*, *171*(1-4), 79-89, doi: 10.1016/j.sedgeo.2004.05.011.

von Eynatten, H., R. Tolosana-Delgado, and V. Karius (2012), Sediment generation in modern glacial settings: Grain-size and source-rock control on sediment composition, *Sedimentary Geology*, *280*, 80-92, doi: 10.1016/j.sedgeo.2012.03.008.

Walter, M. J., T. W. Sisson, and D. C. Presnall (1995), A Mass Proportion Method for Calculating Melting Reactions and Application to Melting of Model Upper-Mantle Lherzolite, *Earth Planet Sc Lett*, *135*(1-4), 77-90, doi: 10.1016/0012-821x(95)00148-6.

Watkins, J., J. Grotzinger, N. Stein, S. Banham, S. Gupta, D. Rubin, K. Stack, and K. Edgett (2016), Paleotopography of Erosional Unconformity, Base of Stimson Formation, Gale Crater, Mars, paper presented at 47th Lunar and Planetary Science Conference, LPI, Houston, TX, Abs. #2939.

Weinberger, R. (1999), Initiation and growth of cracks during desiccation of stratified muddy sediments, *Journal of Structural Geology*, *21*(4), 379-386, doi: 10.1016/S0191-8141(99)00029-2.

Weltje, G. J. (2004), A quantitative approach to capturing the compositional variability of modern sands, *Sedimentary Geology*, *171*(1-4), 59-77, doi: 10.1016/j.sedgeo.2004.05.010.

Weltje, G. J., and H. von Eynatten (2004), Quantitative provenance analysis of sediments: review and outlook, *Sedimentary Geology*, *171*(1-4), 1-11, doi: 10.1016/j.sedgeo.2004.05.007.

White, W. A. (1961), Colloid Phenomena in Sedimentation of Argillaceous Rocks, *Journal of Sedimentary Petrology*, *31*(4), 560-570.

Whitmore, G. P., K. A. W. Crook, and D. P. Johnson (2004), Grain size control of mineralogy and geochemistry in modern river sediment, New Guinea collision, Papua New Guinea, *Sedimentary Geology*, *171*(1-4), 129-157, doi: 10.1016/j.sedgeo.2004.03.011.

Williams, R. M., et al. (2013), Martian fluvial conglomerates at Gale crater, *Science*, *340*(6136), 1068-1072, doi: 10.1126/science.1237317.

Wittmann, A., R. L. Korotev, B. L. Jolliff, A. J. Irving, D. E. Moser, I. Barker, and D. Rumble (2015), Petrography and composition of Martian regolith breccia meteorite Northwest Africa 7475, *Meteoritics & Planetary Science*, *50*(2), 326-352, doi: 10.1111/maps.12425.

Worden, R., and S. Burley (2003), Sandstone diagenesis: the evolution of sand to stone, *Sandstone Diagenesis: Recent and Ancient*, 1-44.

Wray, J. J., S. T. Hansen, J. Dufek, G. A. Swayze, S. L. Murchie, F. P. Seelos, J. R. Skok, R. P. Irwin, and M. S. Ghiorso (2013), Prolonged magmatic activity on Mars inferred from the detection of felsic rocks, *Nat Geosci*, *6*(12), 1013-1017, doi: 10.1038/ngeo1994.

Yen, A. S., et al. (2005), An integrated view of the chemistry and mineralogy of martian soils, *Nature*, *436*(7047), 49-54, doi: 10.1038/nature03637.

Young, G. M., and H. W. Nesbitt (1999), Paleoclimatology and provenance of the glaciogenic Gowganda Formation (Paleoproterozoic), Ontario, Canada: A chemostratigraphic approach, *Geological Society of America Bulletin*, *111*(2), 264-274, doi: 10.1130/0016-7606(1999)111<0264:Papotg>2.3.Co;2.